

Histology-derived volumetric annotation of the human hippocampal subfields in postmortem MRI



Daniel H. Adler ^{a,b,*}, John Pluta ^{a,c}, Salmon Kadivar ^a, Caryne Craige ^a, James C. Gee ^a, Brian B. Avants ^a, Paul A. Yushkevich ^a

^a Penn Image Computing and Science Laboratory (PICSL), Department of Radiology, University of Pennsylvania, 3600 Market Street, Suite 370, Philadelphia, PA 19104, USA

^b Department of Bioengineering, University of Pennsylvania, USA

^c Center for Functional Neuroimaging, Department of Neurology, University of Pennsylvania, USA

ARTICLE INFO

Article history:

Accepted 29 August 2013

Available online 12 September 2013

Keywords:

Hippocampus

Subfields

Histology

MRI

Reconstruction

Postmortem

ABSTRACT

Recently, there has been a growing effort to analyze the morphometry of hippocampal subfields using both *in vivo* and postmortem magnetic resonance imaging (MRI). However, given that boundaries between subregions of the hippocampal formation (HF) are conventionally defined on the basis of microscopic features that often lack discernible signature in MRI, subfield delineation in MRI literature has largely relied on heuristic geometric rules, the validity of which with respect to the underlying anatomy is largely unknown. The development and evaluation of such rules are challenged by the limited availability of data linking MRI appearance to microscopic hippocampal anatomy, particularly in three dimensions (3D). The present paper, for the first time, demonstrates the feasibility of labeling hippocampal subfields in a high resolution volumetric MRI dataset based directly on microscopic features extracted from histology. It uses a combination of computational techniques and manual post-processing to map subfield boundaries from a stack of histology images (obtained with 200 μm spacing and 5 μm slice thickness; stained using the Kluver-Barrera method) onto a postmortem 9.4 Tesla MRI scan of the intact, whole hippocampal formation acquired with 160 μm isotropic resolution. The histology reconstruction procedure consists of sequential application of a graph-theoretic slice stacking algorithm that mitigates the effects of distorted slices, followed by iterative affine and diffeomorphic co-registration to postmortem MRI scans of approximately 1 cm-thick tissue sub-blocks acquired with 200 μm isotropic resolution. These 1 cm blocks are subsequently co-registered to the MRI of the whole HF. Reconstruction accuracy is evaluated as the average displacement error between boundaries manually delineated in both the histology and MRI following the sequential stages of reconstruction. The methods presented and evaluated in this single-subject study can potentially be applied to multiple hippocampal tissue samples in order to construct a histologically informed MRI atlas of the hippocampal formation.

© 2013 Elsevier Inc. All rights reserved.

Introduction

The human hippocampal formation (HF) is a complex and inhomogeneous anatomical region in the medial temporal lobe (MTL) that is essential in the declarative memory system, which encompasses stored events and personal experiences (episodic memory) and explicit facts and concepts (semantic memory) (Amaral and Lavenex, 2007; Duvernoy, 2005; Squire et al., 2004; Zola-Morgan and Squire, 1993). Amaral and Lavenex (2007) define the HF as a “functional brain system” with characteristic unidirectional connectivity, and formed by the hippocampus proper (which is further divided into the cornu Ammonis subfields CA1, CA2, and CA3), the dentate gyrus (DG), the subiculum (SUB), the

presubiculum, the parasubiculum, and the entorhinal cortex (ERC). The structures and subfields forming the HF are known to be differentially and selectively affected by multiple diseases and disorders, as well as by the normal processes of aging (Braak and Braak, 1991; Mueller and Weiner, 2009; Small et al., 2011; West et al., 1994). In addition, they are thought to serve specialized functions in the memory system, including pattern separation and completion by DG and CA3 (Bakker et al., 2008; Leutgeb et al., 2007; Yassa et al., 2010) and novelty detection and allocentric encoding by CA1 (Lisman and Otmakhova, 2001; Suthana et al., 2009). Additionally, hippocampal function is believed to be partially specialized along its longitudinal axis (Fanselow and Dong, 2010; Poppenk and Moscovitch, 2011; Small et al., 2001; Strange et al., 1999) and between hemispheres of the brain (Milner et al., 1997; Nunn et al., 1999; Rosazza et al., 2009).

The HF is frequently targeted in magnetic resonance imaging (MRI) studies due to its important roles in memory formation and retrieval, its hypothesized involvement in other areas, such as spatial memory and

* Corresponding author at: Penn Image Computing and Science Laboratory (PICSL), Department of Radiology, University of Pennsylvania, 3600 Market Street, Suite 370, Philadelphia, PA 19104, USA. Fax: +1 215 615 3681.

E-mail address: danadler@seas.upenn.edu (D.H. Adler).

navigation (Bird and Burgess, 2008; Burgess et al., 2002), and its implication in many diseases and disorders. Neurological and psychiatric conditions known to affect the HF include Alzheimer's disease (AD), temporal lobe epilepsy (TLE), vascular disease, schizophrenia, and post-traumatic stress disorder, with reduced hippocampal volume well documented in studies of the majority of these conditions (Barnes et al., 2009; Geuze et al., 2004; Small et al., 2011). The effects of these conditions on the HF are different and non-uniform. For instance, AD pathology exhibits well-characterized topological selectivity, with ERC and the CA1 subfield affected earliest in the course of the disease (Bobinski et al., 1998; Braak and Braak, 1991; Braak et al., 2006; Gómez-Isla et al., 1996; Price et al., 2001). It has therefore been hypothesized that more focal measurements of volume changes in the HF sub-regions may lead to imaging biomarkers with improved biological relevance and diagnostic and prognostic accuracy over whole-hippocampal measures (Jack et al., 2011; Mueller and Weiner, 2009; Pluta et al., 2012).

Indeed, recent years have evidenced increasing interest in obtaining accurate measurements of subfield-level changes from *in vivo* MRI. Table 1 lists *in vivo* imaging studies that make inferences about hippocampal subregions by labeling them in high-resolution MRI. In each study, hippocampal subregions were manually delineated either directly in all of the subjects' images, or on a core atlas dataset, which was then used to automatically propagate the segmentation to the subjects' images (Hanseeuw et al., 2011; Van Leemput et al., 2009). Given the limitations of the MRI resolution, manual segmentation is forced to rely on macroscopic features. Manual segmentation protocols are typically sets of heuristic rules that declare where to draw boundaries between subfields on the basis of anatomical landmarks, intensity changes, and geometric features. A great deal of variability exists among the proposed rules of HF subregion parcellation in MRI, as evident from the differences in the nomenclature summarized in Table 1 and by select examples of published parcellation results shown in Fig. 1.

By contrast, the neuroanatomy literature defines the boundaries between hippocampal subregions strictly on the basis of microscopic features, such as somatic size, shape and density (Amaral and Lavenex, 2007; Duvernoy, 2005; Harding et al., 1998; Lorente de Nó, 1934; West and Gundersen, 1990). For instance, the transition between

the CA1 and CA2 subfields is characterized by increased density of pyramidal cells with larger and more ovoid somata. In some cases, changes in cytoarchitecture translate into changes in MRI signal. Specifically, hypo-intensity in T2-weighted MRI corresponds to the hippocampal strata that lie along the interface between DG on one side and CA1, CA2, and SUB on the other. However, other subfield boundaries, such as the CA1/SUB and CA3/DG transitions, have no known MRI signature. Indeed, it has been argued that the locations of these cytoarchitectonic boundaries vary greatly across subjects and in most cases do not have a well understood correspondence with macroscopic features or anatomical landmarks that can be extracted from MRI (Amunts et al., 2005; van Strien et al., 2011).

In order to evaluate the validity of existing rule-based MRI subfield parcellation protocols, as well as to derive more anatomically valid protocols in the future, a better way of linking microscopic and macroscopic features in the HF is needed than the current state of the art, which relies on printed atlases that show side-by-side MRI scans and histological slices acquired at different locations in the HF (e.g. Duvernoy, 2005). Specifically, since HF subfield segmentation in MRI is inherently a three-dimensional (3D) problem, it is crucial to develop 3D references of the HF that link cytoarchitectonic boundaries to MRI appearance and that can be sliced virtually along any direction. Furthermore, such references ought to capture the anatomical variability in the population.

High-resolution *ex vivo* MRI microscopy, which occupies a space between the histological modalities used by professional neuroanatomists and the *in vivo* MRI used by neuroimagers, has excellent potential to provide such reference datasets. By taking advantage of ultra-high field strengths (7 T and above), long acquisition times, many signal excitations, and focused fields of view, postmortem studies of the HF (summarized in Table 2) realize enormous gains in image quality over *in vivo* MRI, and allow excellent visualization of hippocampal lamina as well as clear differentiation between the HF and adjacent gray matter structures. However, even at the resolution and contrast of *ex vivo* MRI, the boundaries between subfields are not all visually discernible (Chakeres et al., 2005; Yushkevich et al., 2009).

This paper represents an intermediate step toward a long-term vision of building a postmortem MRI and histology atlas of the HF. It demonstrates the feasibility of mapping HF subfield boundaries from a

Table 1

In vivo, high-resolution MRI studies of the hippocampal subfields.

Study	Field (T)	Field (T)	Sequence	Resolution before interpolation (mm ^a)	No. slices/coverage (cm)	Duration (min)	Segmentation labels in HF
Wang et al. (2003)	1.5	T1, MPAGE		1.0 × 1.0 × 1.0	(Whole brain)	11.0	CA1, CA2, CA3, CA4 ^b , DG, SUB, alveus/fimbria ^c
Apostolova et al. (2006)	1.5	T1, SGE		0.86 × 1.15 × 1.5	(Whole brain)	N.A.	CA1, CA2, CA3, SUB ^{a,c}
Kirwan et al. (2007)	3	T1, MPAGE		0.75 × 0.75 × 0.75	60/4.5	N.A.	CA1, CA3/DG, SUB
Van Leemput et al. (2009)	3	T1, MPAGE		0.38 × 0.38 × 0.8	208/16.6 (whole brain)	36.7	CA1, CA2/3, CA4/DG, SUB, pre-SUB, fimbria
Hanseeuw et al. (2011)	3	T1, GRE		0.81 × 0.95 × 1.0	150/15.0 (whole brain)	8.2	Same as Van Leemput et al. (2009) ^d
La Joie et al. (2010)	3	PD		0.375 × 0.375 × 2.0	13/5.2	7.6	CA1, CA2/3/4/DG, SUB
Shing et al. (2011)	3	PD, FSE		0.4 × 0.4 × 2.0	30/6.0	N.A.	CA1/2, CA3/4/DG, SUB ^e
Bonci et al. (2012)	3	T2, FSE		0.52 × 0.52 × 0.5	104/5.2	12.0	CA1, CA3, DG, SUB
Zeineh et al. (2000)	3	T2, FSE		0.39 × 0.39 × 3.0	16/4.8	N.A.	CA1, CA2/3/DG ^f , SUB, ERC, PRC
Ekstrom et al. (2009)	3	T2, FSE		0.4 × 0.4 × 1.0	36/3.6	6.4	Same as Zeineh et al. (2000)
Winterburn et al. (2013)	3	T1, FSGRE		0.57 × 0.57 × 0.6	118	20	CA1, CA2/3, CA4/DG, SUB, SRLM
		T2, FSE			118	16	
Mueller et al. (2007)	4	T2, FSE		0.4 × 0.5 × 2.0	24/4.8	5.5	CA1, CA2, CA3/4/DG, SUB, ERC ^e
Yushkevich et al. (2010)	4	T2, FSE		0.4 × 0.5 × 2.0	24/4.8	3.4	CA1, CA2, CA3, DG, SUB, ERC, PHG ^g
Malykhin et al. (2010)	4.7	T2, FSE		0.52 × 0.68 × 1.0	90/9.0	13.5	CA1/2/3, DG, SUB
Henry et al. (2011)	7	T2, FSE		0.25 × 0.25 × 1.2	54/6.5	N.A.	CA1/2/3, CA4/DG ^e
Wisse et al. (2012)	7	T2, 3D FSE		0.7 × 0.7 × 0.7	N.A.	N.A.	CA1, CA2, CA3, CA4/DG, SUB, ERC

MPAGE: magnetization prepared rapid gradient echo; SGE: spoiled gradient echo; GRE: gradient echo; FSE: fast/turbo spin echo; FSGRE: fast spoiled GRE; SRLM: stratum radiatum and stratum lacunosum-moleculare; PHG: parahippocampal gyrus.

^a Subfields labeled on HF surface mesh only.

^b The dentate hilus (polymorphic layer of DG) is referred to as CA4 by some authors (Duvernoy, 2005).

^c Analysis performed on HF surface only (i.e. no subfield volumetry performed).

^d Segmented using automatic method of Van Leemput et al. (2009).

^e Segmentation not done in hippocampal head.

^f Combined CA/DG label used in most anterior and posterior sections.

^g Segmentation done only in hippocampal body.

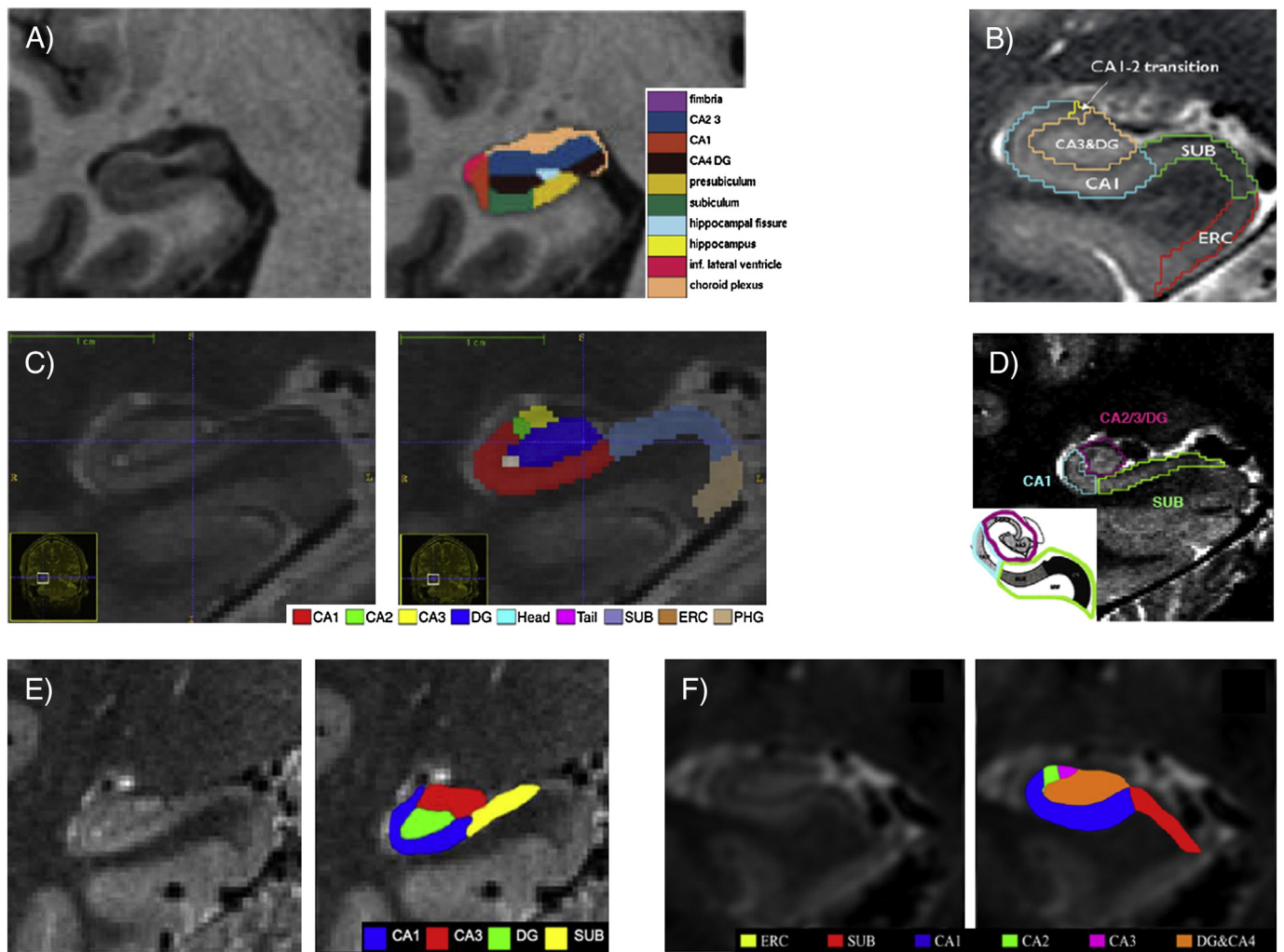


Fig. 1. Examples of MRI segmentation protocols of hippocampal subfields: (A) Van Leemput et al. (2009), (B) Mueller and Weiner (2009), (C) Yushkevich et al. (2010), (D) La Joie et al. (2010), (E) Bonnici et al. (2012), (F) Wisse et al. (2012).

Images reproduced with permission from publishers.

stack of histological slices acquired densely along the full anterior-posterior extent of the HF onto a volumetric postmortem MRI scan of the intact, whole HF. The result of this mapping is a parcellation of the MRI volume that is based on actual cytoarchitectonic boundaries, rather than boundaries inferred from heuristic rules. To our knowledge, this is the first time that a full 3D parcellation of HF subfields in an MRI scan has been done using histologically-derived boundaries. The mapping methodology presented in this paper complements our earlier work (Yushkevich et al., 2009) that combined postmortem MRI scans

from multiple tissue samples into a probabilistic atlas, but did not use histology.

The remainder of the paper is organized as follows. We first review prior work on ex vivo MRI of the hippocampal subfields and 3D histology reconstruction. We then describe the histology and MRI acquisition procedures, the histology segmentation procedure, and the histology reconstruction methods. Finally, we evaluate reconstruction accuracy and present a visual summary and discussion of the reconstruction and volumetric annotation of the hippocampal subfields in MRI.

Table 2

Ex vivo, high-resolution MRI studies of the hippocampal subfields.

Study	Field (T)	Sequence	Resolution (mm^3)	Coverage	Duration (h)
Wiesmann et al. (1999)	7	T2, SE	$0.064 \times 0.064 \times 1.0$	Single slice	N.A.
Fischl et al. (2009)	7	T2*, MEF	$0.1 \times 0.1 \times 0.1$	Whole HF	N.A.
Augustinack et al. (2010)	7	T2*, FLASH	$0.1 \times 0.1 \times 0.1$	Whole HF	17
	4.7	DTI, SE	$0.2 \times 0.2 \times 0.2$	Whole HF	40
Chakeres et al. (2005)	8	T1/T2, SE	$0.21 \times 0.21 \times 2.0$	Single slice	0.05
Fatterpekar et al. (2002)	9.4	PD/T2, SE	$0.078 \times 0.078 \times 0.5$	Single slice	14.3
Yushkevich et al. (2009) ^a	9.4	PD/T2, FSE	$0.3 \times 0.2 \times 0.2, 0.2 \times 0.2 \times 0.2$	Whole HF	13.2–15.5, 62.5
Shepherd et al. (2007)	14.1	DTI, SE	$0.06 \times 0.06 \times 0.3$	Whole HF	19.2

SE: spin echo; MEF: multi-echo FLASH.

^a Segmentation performed manually for CA1, CA2, CA3, CA4/DG, SUB, and ERC in hippocampal body (Yushkevich et al., 2010).

Prior work

Structural ex vivo MRI of the hippocampal subfields

Table 2 summarizes several ex vivo MRI studies of hippocampal subfields. Varying sequence parameters have been chosen to optimize postmortem image contrast, with values depending greatly on the nature and duration of tissue fixation, as well as the use of exogenous contrast agents. Physical and chemical changes during fixation cause T1 and T2 relaxation rates to decrease and to converge within gray and white matter of the postmortem brain with increased fixation time (Blamire et al., 1999; Dawe et al., 2009; Pfefferbaum et al., 2004). As a result, proton spin density (PD) weighting and intermediate PD/T2 weightings have been shown to improve gray and white matter contrast over T2 weighting in postmortem studies.

Initial studies looked at individual slices or tissue slabs extracted from the HF (Chakeres et al., 2005; Fatterpekar et al., 2002; Wiesmann et al., 1999). More recently, imaging of the full 3D extent of the hippocampal region was performed with isotropic 0.1 mm³ resolution at 7 T by Fischl et al. (2009) and Augustinack et al. (2010). Fischl et al. (2009) used features visible in their high-field, high-resolution images to segment borders of the ERC, which were then mapped to 1 mm³ in vivo 1.5 T images and to a cortical surface model. They showed that microscopically-defined ERC borders could be accurately localized using cortical folding patterns. Augustinack et al. (2010) performed fiber tracking of the perforant pathway that connects ERC to DG in high-resolution, 4.7 T diffusion tensor images (DTI), validating their results with co-registered 7 T, 0.1 mm³ structural images and reconstructed histology. High-resolution DTI has been used by other groups to study diffusion characteristics of hippocampal subfields and pathways (Shepherd et al., 2007; Zeineh et al., 2012).

Yushkevich et al. (2009) created a postmortem MRI atlas of the HF by normalizing manually labeled images from five specimens acquired at 9.4 T with nearly isotropic 0.2 mm³ resolution. Unlike the present work, subfields in Yushkevich et al. (2009) were labeled in MRI space based on macroscopic features. Using shape-based normalization to in vivo images, the atlas was applied to a study of subfield-specific atrophy in TLE (Das et al., 2011).

Multiple studies have compared MRI to histological sections in order to confirm anatomical findings seen in the former modality (Augustinack et al., 2010; Chakeres et al., 2005; Fatterpekar et al., 2002; Fischl et al., 2009; Wiesmann et al., 1999). These comparisons were made with selected 2D histological sections and not with full 3D reconstructions. While it does not have near the resolution or contrast of histology, ex vivo high-field MRI does yield far superior contrast and much smaller voxels compared to in vivo MRI. As such, ex vivo MRI can potentially serve as an intermediate modality between histology and in vivo MRI, helping to better understand the characteristics of the latter (Thomas et al., 2008).

Volumetric histology reconstruction

Other groups have created 3D biological models and atlases from MRI and histological imaging of the same subject. This has been done in the whole human brain (Amunts et al., 2013; Toga et al., 1997), the human basal ganglia and thalamus (Chakravarty et al., 2006; Krauth et al., 2010; Yelnik et al., 2007), the primate brain (Cannestra et al., 1997; McLaren et al., 2009; Newman et al., 2009; Saleem and Logothetis, 2012), and the mouse brain (Leenberg et al., 2010; Lein et al., 2006; Li et al., 2009; MacKenzie-Graham et al., 2004). Amunts et al. (2005) used 3D reconstructed histology from 20 postmortem specimens to create probabilistic cytoarchitectonic maps that included the hippocampal formation and its division into the cornu Ammonis, dentate gyrus (including CA4), and the subiculum complex. Reconstruction was guided by block-face photographs and by whole-brain, postmortem T1-weighted MRI acquired at 1.5 T and roughly 1 mm³

isotropic resolution. However, their delineations were performed on a relatively small number of histological sections (<20) and did not include the CA subfields or the SRLM-HS.

Additionally, histology reconstruction has been applied to localize targets for surgical planning (Bardinet et al., 2009; Purger et al., 2009), to map white matter tracts (Bürgel et al., 1999; Dauguet et al., 2007b), to evaluate the extent of pathology (Groen et al., 2010; Meyer et al., 2006; Park et al., 2008; Xiao et al., 2011), and to analyze response to therapy (Breen et al., 2005b). Reconstruction methods have also been applied to autoradiographic sections, where it has been used in the validation of brain function and metabolism (Hess et al., 1998; Leenberg et al., 2010; Malandain et al., 2004).

The methods used in our paper are extensions of our group's prior work on whole mouse brain histology reconstruction (P. Yushkevich et al., 2006), in which we created a 3D anatomical reference image for the Allen Brain Atlas of the Allen Institute for Brain Sciences (Lein et al., 2006). This is a genome-wide database of gene expression in the mouse brain that allows researchers to relate gene expression and neuroanatomy.

In its most basic form, reconstruction of histological slices can be reduced to 2D inter-slice registration followed by slice stacking. In practice, however, this often leads to incorrect reconstruction, as 2D inter-slice registration does not explicitly account for true 3D tissue shape and coherence that are lost during microtomy. Histology inter-slice registration is also error-prone, further frustrating reconstruction. Registration errors may result from differences in slice thickness, sectioning angle, immunohistochemical staining intensity, as well as inherent discontinuities in anatomy between slices (Breen et al., 2005a; Malandain et al., 2004; Simmons and Swanson, 2009). Artifacts that occur during microtomy and slide mounting (e.g. tissue shrinking, tearing, shearing, folding, and displacement) are variable between slices and can also lead to poor inter-slice registration. Even small misalignments between neighboring slices can accumulate, thereby distorting and offsetting shapes along the slice stacking dimension (Beare et al., 2008; Nikou et al., 2003).

The global shape information lost during sectioning can be reintroduced during reconstruction via co-registration to another modality, as has been done using in vivo (Ceritoglu et al., 2010; Dauguet et al., 2007a; Malandain et al., 2004) and ex vivo MRI (Choe et al., 2011; Ourselin et al., 2001a; P. Yushkevich et al., 2006). If the MRI is performed in situ, then this co-registration step can potentially correct distortions that arise due to loss of support and vascular pressure following tissue extraction (Park et al., 2008). Fixation and embedding lead to dehydration that also significantly alters tissue shape and volume (Breen et al., 2005a; Schormann et al., 1995). Block-face photographs taken during tissue sectioning often serve as an additional intermediate modality to guide reconstruction or alignment to the MRI reference (Chakravarty et al., 2006; Dauguet et al., 2007a; Yelnik et al., 2007).

In the absence of a reference volume or adequate prior shape knowledge, reconstruction results may be biased. For instance, curved structures may end up straightened following slice stacking—the so-called z-shift or banana problem (Beare et al., 2008; Malandain et al., 2004). Several techniques have been applied to mitigate the absence of a reference volume, including block-matching (Ourselin et al., 2001b), registration to a designated reference slice (Cifor et al., 2009; Malandain et al., 2004), registration within particular slice neighborhoods (Arganda-Carreras et al., 2010; P. Yushkevich et al., 2006), minimization of energy functionals and physics-based approaches that account for complex inter-slice effects (Feuerstein et al., 2011; Gefen et al., 2003; Guest and Baldock, 1995; Krinidis et al., 2003; Nikou et al., 2003), and the imposition of smoothness constraints between slices (Cifor et al., 2009; Ju et al., 2006). The reconstruction literature demonstrates a broad range of methods for inter-slice and volumetric co-registration, including the use of fiducial markers (Beare et al., 2008; Breen et al., 2005b), landmarks or extracted features (Gefen et al., 2003; Rangarajan et al.,

1997), block-matching (Ourselin et al., 2001b; Pitiot et al., 2006), and a large variety of transformation models. Further reviews of histology reconstruction are presented by Arganda-Carreras et al. (2010), Ceritoglu et al. (2010), Cifor et al. (2009), and Ju et al. (2006).

Materials and methods

Specimens and imaging

We studied the formalin-fixed (≥ 21 days) brain from the autopsy case of an 89-year-old female with no abnormal neuropathological findings. The specimen was obtained from the National Disease Research Interchange (Philadelphia, PA). We extracted a tissue sample measuring approximately $2 \times 3 \times 8 \text{ cm}^3$ from the right hemisphere and containing the intact, whole hippocampal formation.

An MRI of the whole HF sample was obtained on a 9.4 T, 31 cm horizontal bore Varian scanner (Agilent Technologies, Inc., Santa Clara, CA) using a 70 mm transmit/receive volume coil (inner diameter TEM coil, Insight Neuroimaging Systems, Worcester, MA). In order to prevent susceptibility artifacts due to tissue-air interfaces, the sample was immersed in a plastic cylinder containing a perfluoropolyether that yields almost no detectable MRI signal. The cylinder was carefully agitated and tapped to dislodge air bubbles trapped on the sample's surface, then wrapped with foam and fit snugly inside the imaging coil. A standard spin echo multi-slice (SEMS) sequence was acquired along an oblique slice plane parallel to the longitudinal axis (readout direction) of the hippocampus, with TR/TE = 5 s/23 ms, and 48 signal averages. Relatively long TR and short TE were used to account for the effects of long-term formalin fixation, which causes significant reduction in T1 and T2 relaxation times in brain tissue (Blamire et al., 1999; Dawe et al., 2009; Pfefferbaum et al., 2004; Yong-Hing et al., 2005). The raw matrix size was $200 \times 500 \times 128$ voxels with 0.16 mm^3 isotropic resolution. Image acquisition took 13.33 h.

Since the HF sample was too large for histological processing, it was further sectioned into six uniformly spaced sub-blocks oriented roughly perpendicular the longitudinal axis. An MRI was then acquired of the sub-blocks using a similar sequence as for the intact sample: Each sub-block was placed in a plastic histology cassette and immersed in the perfluoropolyether compound prior to scanning using the SEMS sequence with TR/TE = 4 s/23 ms, 80 signal averages, and 0.20 mm^3 isotropic resolution. Acquisition time was approximately 2 h per sub-block. The MRI z-plane was oriented parallel to the plane along which the sub-blocks were sectioned. These sub-block MRIs served as references to guide subsequent 3D histology reconstruction.

Following MRI acquisition, the tissue underwent histological processing. Each tissue sub-block was embedded in paraffin and sectioned on a microtome into slices of $5 \mu\text{m}$ thickness parallel to the block face. Histology slice spacing was $200 \mu\text{m}$, so as to match the sub-block MRI resolution. The sections were mounted on slides and histochemically stained using the Kluver-Barrera method (luxol fast blue counterstained with cresyl violet) (Kluver and Barrera, 1953), which highlights the Nissl substance in neuronal cell bodies as pink-violet, and myelin in axons as blue-green. The slides were scanned and digitized at $0.5 \mu\text{m}/\text{pixel}$ resolution with an Aperio ScanScope CS system (Aperio Technologies, Inc., Vista, CA). Fig. 2 summarizes the imaging protocol.

Histology image pre-processing

The digitized histology slides were downsampled to 1% ($50 \mu\text{m}/\text{pixel}$) of their original size in each dimension in order to facilitate reconstruction. All subsequent processing steps were performed on the downsampled images, as they retained high contrast of salient anatomical structures and a sufficient level of detail to guide registration.

To prevent dislodged tissue fragments and other debris from influencing subsequent image registration and reconstruction, the foreground was automatically segmented from background and debris in

each histology slide. Foreground segmentation was performed on grayscale intensity images obtained via the luminance transform $0.30R + 0.59G + 0.11B$ on the red, green, and blue color channel intensities. We used Atropos, an n -class Markov random field segmentation software package (Avants et al., 2011), to segment the slides into three label classes (using 1.0 smoothing factor and one voxel neighborhood size). The label masks were assigned to white matter, gray matter, and background. The white and gray matter labels were united into a foreground tissue mask, for which we retained only the largest connected component.

To compensate for staining differences, the intensity ranges of the RGB channels were independently scaled and shifted between slices using linear intensity mappings. Let $\mu_i^{k,\text{WM}}$ and $\mu_i^{k,\text{GM}}$ denote the mean white and gray matter intensities for color channel $k \in \{\text{R}, \text{G}, \text{B}\}$ of histology slice $i \in [1, N]$. These values were computed using the segmentation masks described above. The optimal slope a_i^k and intercept b_i^k used to map color channel k of slice i were then computed as the minimizers of the following function:

$$E(\mathbf{a}^k, \mathbf{b}^k) = \sum_{i=1}^N \left((a_i^k \cdot \mu_i^{k,\text{GM}} + b_i^k) - (a_{i+1}^k \cdot \mu_{i+1}^{k,\text{GM}} + b_{i+1}^k) \right)^2 + \left((a_i^k \cdot \mu_i^{k,\text{WM}} + b_i^k) - (a_{i+1}^k \cdot \mu_{i+1}^{k,\text{WM}} + b_{i+1}^k) \right)^2, \quad (1)$$

where $\mathbf{a}^k = (a_1^k, \dots, a_N^k)$, $\mathbf{b}^k = (b_1^k, \dots, b_N^k)$, $\mu_{N+1}^{k,\text{GM}} \equiv \mu_1^{k,\text{GM}}$, and $\mu_{N+1}^{k,\text{WM}} \equiv \mu_1^{k,\text{WM}}$. Parameters of the central reference slice $R = \lfloor N/2 \rfloor$ of each sub-block were set to identity: $a_R^k = 1$, $b_R^k = 0$.

Graph-theoretic slice stacking

The first stage of the histology reconstruction pipeline consisted of inter-slice co-registration and stacking to create an initial 3D volume. A graph-theoretic approach was used during this stage in order to minimize the propagation of alignment errors and the accumulation of small slice shifts along the stacking (or z) dimension (Yushkevich et al., 2006a). We applied these methods to reconstruct each histology sub-block separately.

Let $\{h_1, \dots, h_N\}$ denote the ordered sequence of N gray-scale, downsampled histology slices. First, each slice was co-registered to its neighbors up to k slices away using 2D affine (six degree-of-freedom, DOF) transformations. Thus, slice h_i was registered to neighbors $\{h_{i-k}, \dots, h_{i-1}, h_{i+1}, \dots, h_{i+k}\}$, where $1 + k \leq i \leq N - k$. We used a neighborhood size of $k = 5$ for our experiments. Registration was performed using the Advanced Normalization Tools (ANTs) toolkit (Avants et al., 2008) with the normalized mutual information (NMI) similarity metric. The optimal NMI value between each pair of registered slices, $\text{NMI}(h_i, h_j)$, for $j \in \{i-k, i+k\}$ was stored following each registration.

A weighted graph was then constructed with N vertices representing the slices. Edges between each pair of vertices i and j represented slices registered in the prior step. The edge weight between vertices i and j was set to

$$w_{ij} = w_{ji} = (1 - \text{NMI}(h_i, h_j)) \cdot (1 + \epsilon)^{|i-j|}, \quad (2)$$

where $\text{NMI}(h_i, h_j)$ is the NMI metric (normalized to $[0, 1]$) between slices h_i and h_j . Lower values of NMI correspond to lower similarity following registration; larger values to higher similarity. The edge weights therefore measured the degree of similarity and proximity between slices, with poorer registrations and more distant slices yielding edges with higher weights. The constant ϵ was set to a small positive number: 0.01 for our experiments. This value was chosen empirically to offer the best reconstruction quality for our data.

The graph's edge weights modulated the amount of slice skipping in the concatenated sequences of transformations to the reference. In particular, larger values of the constant ϵ tended to reduce slice skipping by

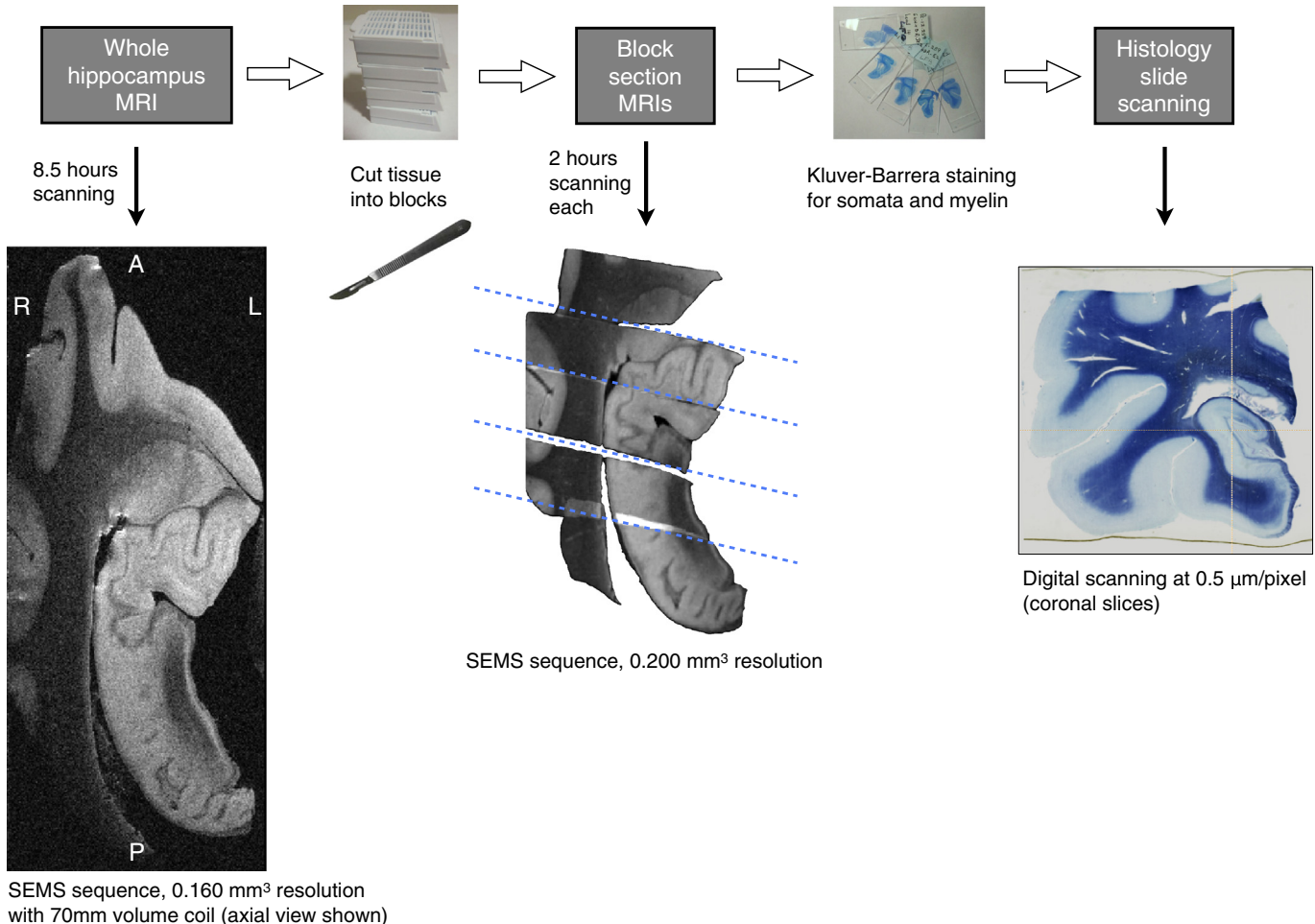


Fig. 2. Postmortem MR and histological imaging protocol of the human hippocampal formation (SEMS: spin echo multi-slice sequence).

weighting edges between distant slices more heavily; smaller values of ϵ encouraged slice skipping. Increased skipping tended to reduce registration error propagation during reconstruction, particularly in cases where certain slices registered poorly to their neighbors. The algorithm thus transformed each slice to the reference by effectively bypassing poorly registered pairs of slices, ultimately mitigating negative effects of distorted slices on reconstruction.

Next, we designated the central histology slice h_R of each sub-block as the reference to which all other slices of the block were

transformed. The least cost edge path was found in the graph from each slice h_i to the reference slice h_R using Dijkstra's algorithm (Fig. 3). Each path represented the sequence of 2D affine transformations mapping the sub-block's slices to the reference, with respect to the defined edge weights. Finally, we concatenated the sequence of transformations from h_i to h_R into a single transformation $T_{i,R}$. Each slice h_i was then transformed and resampled to the space of the reference slice according to $T_{i,R}$. Finally, the slices were stacked into a 3D volume.

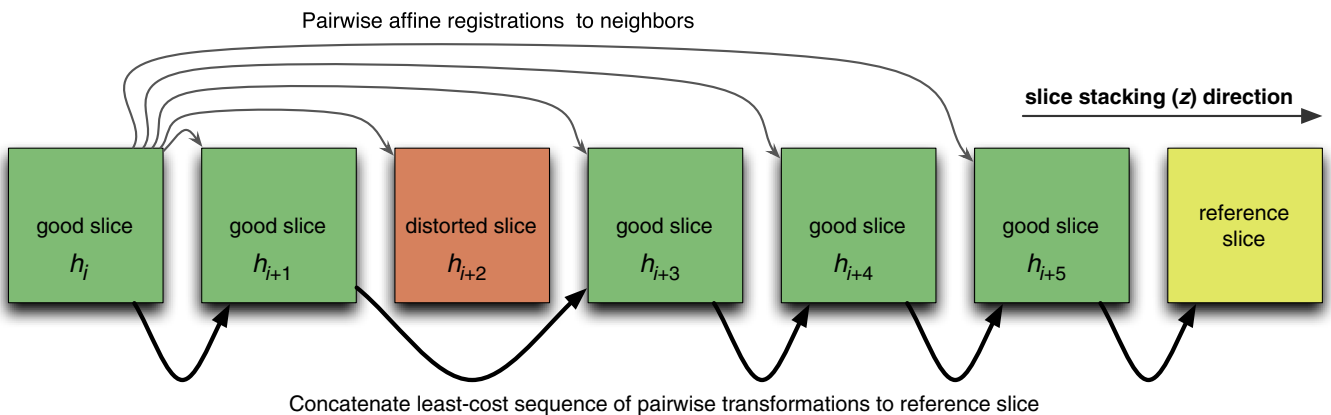


Fig. 3. Schematic of graph-theoretic slice stacking. The least-cost sequence of transformations from slice h_i to the reference slice is concatenated, thereby skipping distorted slices.

Subfield segmentation

Hippocampal subfields were manually segmented along the entire length of the hippocampal formation. The segmentation of the histology data was performed in two stages. In the first stage, Aperio ImageScope software (Aperio Technologies, Inc., Vista, CA) was used to identify and mark transitions between hippocampal subfields in the raw (untransformed) histology images. The actual segmentation (assigning anatomical labels to polygonal regions of interest) was performed on the histology images aligned by the graph-theoretic stacking algorithm ([Graph-theoretic slice stacking](#) section). The advantage of tracing subfields in the aligned images was the consistency in the orientation and position of adjacent slices, which allowed the tracer to follow subfield boundaries from slice to slice more reliably than would be possible in the raw histology data. Furthermore, working with the downsampled images made it possible to use ITK-SNAP ([Yushkevich et al., 2006b](#)) as the segmentation tool, which was more practical than tracing over full-resolution images in ImageScope software. However, when segmenting each aligned downsampled slice, the tracer would refer to the corresponding full-resolution slice in ImageScope.

The histology segmentation used a set of anatomical labels (CA1, CA2, CA3, DG, SUB, and SRLM-HS) similar to those used in in vivo imaging studies of hippocampal structure ([Table 1](#)). This is because the ultimate purpose of this work is to inform in vivo MRI segmentation. Thus, similar to the in vivo literature, multiple neuronal layers (strata) of the hippocampus were grouped together within subfield labels. Specifically, subfield labels CA1, CA2, and CA3 consist of the stratum pyramidale of the hippocampus proper. The label "DG" combines the molecular, granule cell, and polymorphic layers of the DG, as well as the region referred to as CA4 in the convention established by [Lorente de Nó \(1934\)](#) and followed by [Duvernoy \(2005\)](#), but which [Amaral and Lavenex \(2007\)](#) argue should instead be called the hilus of the DG, due to its closer association with the DG than with the hippocampus proper. The remaining strata (stratum radiatum and stratum lacunosum-moleculare of the hippocampus proper) and the vestigial hippocampal sulcus are grouped under the "SRLM-HS" label. The SUB label does not distinguish between presubiculum, parasubiculum and the subiculum proper.

Boundaries between adjacent subfields were determined on the basis of cytoarchitectonic features, rather than geometric or heuristic rules, following the descriptions and depictions of the microscopic characteristics of the subfields (i.e. the size, shape, and density of the neuronal somata) given in Sections 3.2.1 and 3.2.2 of the [Duvernoy \(2005\)](#) atlas. Following this atlas, the CA1 neuronal somata in the pyramidal layer (which stain purple) have an ovoid shape and are populated sparsely ([Fig. 4A](#)). This region also has the thickest pyramidal layer of all the CA subfields. By contrast, the somata in CA2 ([Fig. 4B](#)) are triangular in shape and larger than the somata of CA1. They are also the most densely packed somata of all the CA subfields. In addition, the CA2 pyramidal layer is the thinnest of the CA subfields. A CA1/CA2 transition region, where these characteristics modulate from CA1-like to CA2-like can be identified in the pyramidal cell layer, and the boundary between CA1 and CA2 subfields was drawn at the best visual estimate of the midpoint of this region ([Fig. 5F](#)). The somata in CA3 ([Fig. 4C](#)) are similar in appearance to those in CA2, but are more sparsely packed, and the pyramidal layer is thicker than in CA2. These differences make it possible to identify a CA2/CA3 transition region ([Fig. 5H](#)). The somata in the hilar region of the DG (called CA4 by [Duvernoy \(2005\)](#)) appear similar to those in CA3 but are more ovoid and sparse. The transition between CA3 and the hilus of the DG follows an arc that can be visually identified in many slices ([Fig. 5J](#)). The SRLM-HS label, together with the opened hippocampal sulcus, forms much of the outer boundary for the DG label and the inner boundary for most of the CA subfields and subiculum. The outer CA boundary is clearly marked by the dark blue staining of the adjacent white matter structures (alveus and fimbria). The neuronal somata in the subiculum appear quite similar to those in CA1, but its pyramidal layer is characterized by a more striated appearance ([Fig. 4E](#)). However, the transition between CA1 and the subiculum is typically the most difficult of the transition zones to identify visually. The medial boundary of the SUB label was drawn to the ERC in the histology slices where the ERC was captured; however, many slices cut off the ERC and portions of the subiculum, pre-subiculum and parasubiculum. In those slices, the SUB label was drawn as far medially as possible. The ERC was not segmented as part of this work, since it is not captured in many of the slices and because its six-layered cortical

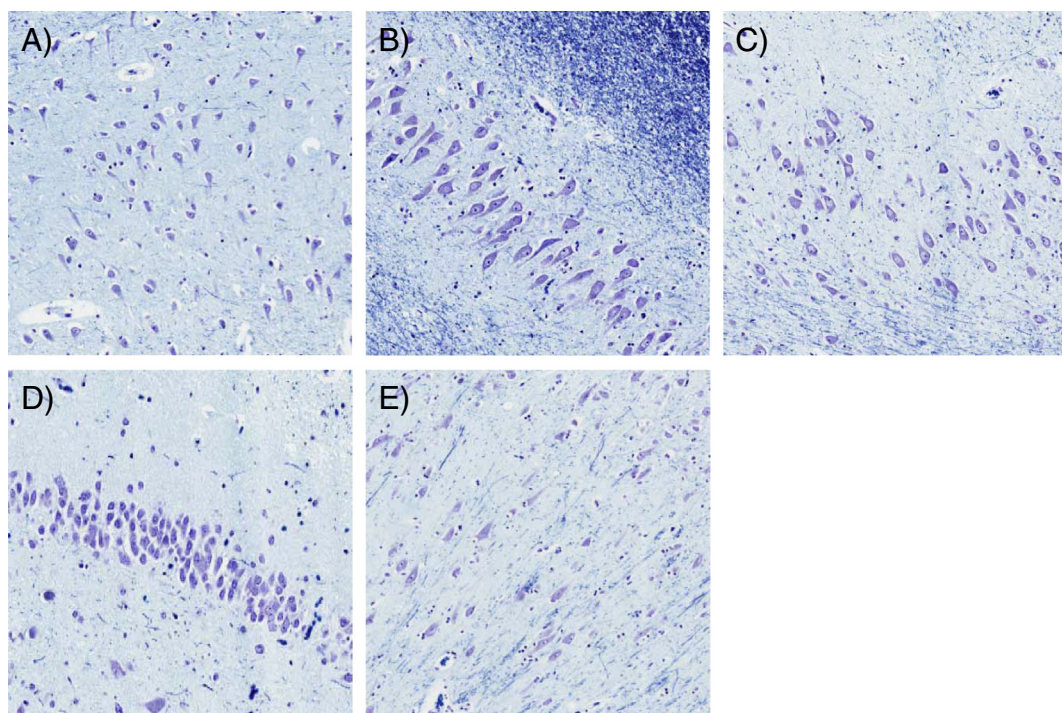


Fig. 4. Zoomed-in views of histology slice displaying cell types in the hippocampal formation: pyramidal cell layer of cornu Ammonis subfields (A) CA1, (B) CA2, (C) CA3; (D) granule cell layer of dentate gyrus (DG); (E) pyramidal cell layer of subiculum.

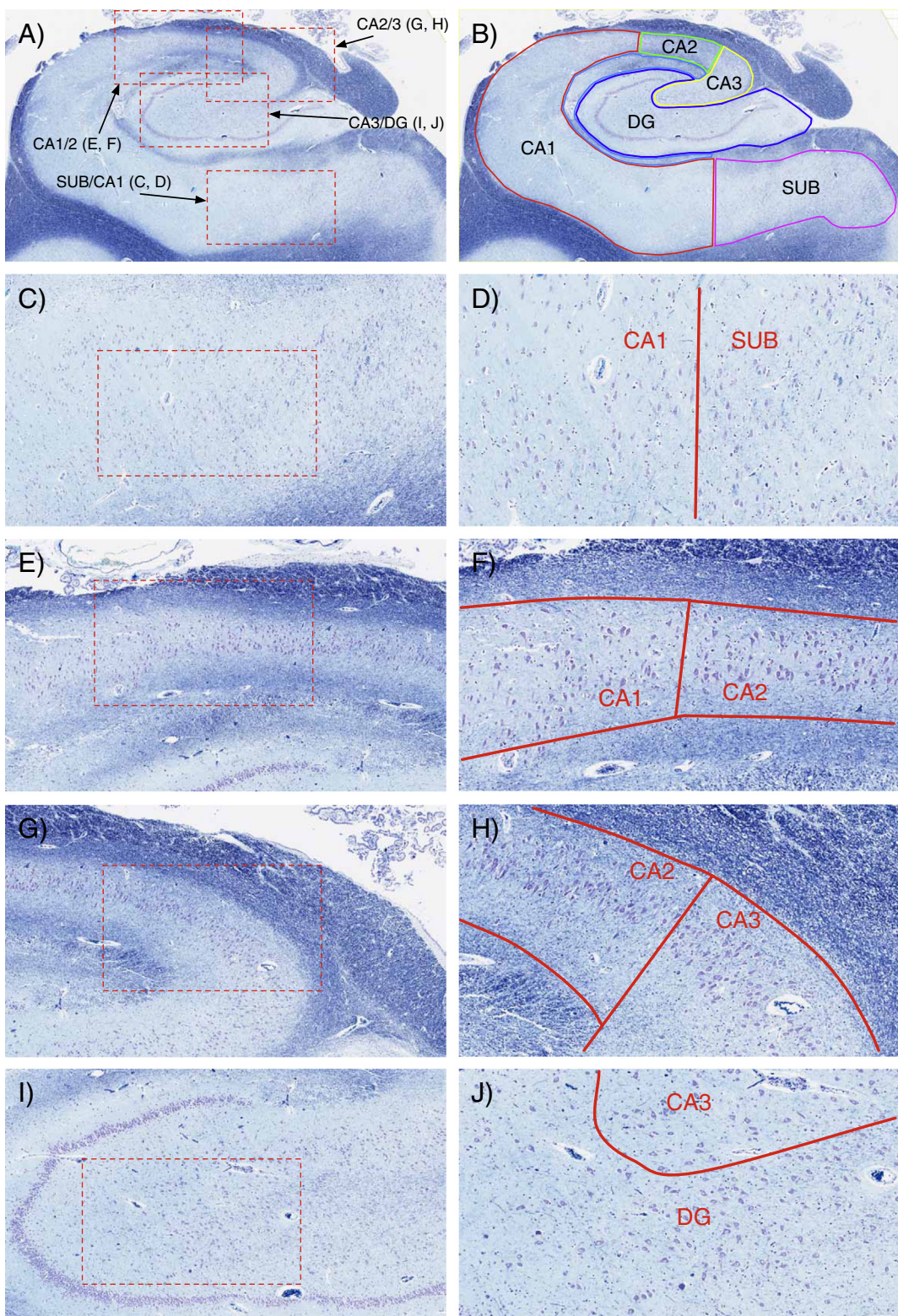


Fig. 5. Histology image of hippocampal body shown (A) with subfield transition regions and (B) full segmentation. Zoomed-in views of transition regions are shown at 5× (left column) and 10× (right column): (C, D) SUB/CA1; (E, F) CA1/CA2; (G, H) CA2/CA3; (I, J) CA3/DG.

structure differs significantly from the three-layered structures of CA and DG.

For completeness, illustrations of the manual segmentation of the histology slices along the anterior to posterior extent of the hippocampus are included in the Supplementary Material.

Histology-MRI co-registration refinement

Though graph-theoretic slice stacking provided a sufficient amount of consistency in orientation and position between slices to permit tracking subfields with consistency along the stack, there remained errors in

reconstruction. Following slice stacking, the main hindrance to accurate reconstruction was “z-shift” error: Even though neighboring slices were well aligned, overall 3D shape along the stacking direction was distorted due to the accumulation of registration errors between slices and the absence of true 3D shape information. Inter-slice alignment during stacking gave good correspondence between local histology features, but the initial reconstruction failed to exactly match the tissue’s 3D shape. To eliminate z-shift, we co-registered the reconstructed histology with the sub-block MRI, the latter of which was assumed to represent true tissue shape. Fig. 6 gives a schematic of the major steps in the reconstruction pipeline.

Let us call H^0 the histology volume following stacking in the previous reconstruction stage (Materials and methods section) and M^0 the sub-block MRI. First, M^0 was registered to H^0 using the NMI similarity metric and a 3D scaling (9-DOF) transformation model, which accounted for global positioning and shape differences between the two modalities (e.g. due to shrinking of the tissue during fixation).

Denote by M^1 the MRI volume after it has been transformed and resampled to the space of H^0 . We then performed a 2D, in-plane affine registration between each slice of H^0 and its corresponding slice (i.e. at the same z position) in M^1 . The transformed slices of H^0 were then re-stacked into a new estimate of the histology volume, which we call H^1 . This 3D/2D registration sequence was iterated (i.e. mapping M^1 to H^1 to yield M^2 and H^2 , etc.).

Convergence was based on registration quality between warped histology and MRI slices. Let h_i^k and m_i^k be the i th slices of the histology (H^k) and MRI (M^k) volumes following k iterations of the algorithm. Registration quality at iteration k was defined as

$$Q(k) = \frac{1}{N} \sum_{i=1}^N \text{NMI}(d_i^k, m_i^k), \quad (3)$$

where N is the total number of slices. Convergence was declared when the relative change in $Q(k)$ fell below a threshold of 10^{-3} in our experiments, which led to between four and seven iterations for the tissue sub-blocks.

Diffeomorphic registration refinement

Following convergence of 3D/2D affine co-registration refinement, we performed 2D diffeomorphic registration refinement between slices of the histology and MRI volumes. This was done in order to further improve reconstruction continuity, to recover residual differences between the modalities, and to recover true tissue shape both in-plane and along the stacking dimension. The registrations at this stage were done using the 2D diffeomorphic, Symmetric Normalization (SyN) transformation model in the ANTs package (Avants et al., 2008) using the following settings: three multi-resolution levels with a maximum of 1000 iterations per level, 0.25 gradient step size, and Gaussian regularization with 3.0 pixel standard deviation.

Let \hat{H}^0 and \hat{M} denote the histology reconstruction and MRI volumes after the previous affine co-registration refinement stage (Histology-MRI co-registration refinement section) has been executed. Each histology slice h_i of \hat{H}^0 was deformed to simultaneously match its adjacent slices h_{i-1} and h_{i+1} , as well as its corresponding MRI slice m_i of \hat{M} , as shown in Fig. 7. The registration of histology slice h_i was done using the following similarity metric:

$$\frac{1-b}{a_{i,i-1} + a_{i,i+1}} \cdot (a_{i,i-1} \cdot \text{NMI}(h_i, h_{i-1}) + a_{i,i+1} \cdot \text{NMI}(h_i, h_{i+1})) + b \cdot (h_i, m_i). \quad (4)$$

Weights $a_{i,i-1}$ and $a_{i,i+1}$ were computed from values in $N_i = \{\text{NMI}(h_i, h_j) \mid j \in [i-5, i+5]\}$, which were obtained in the stacking

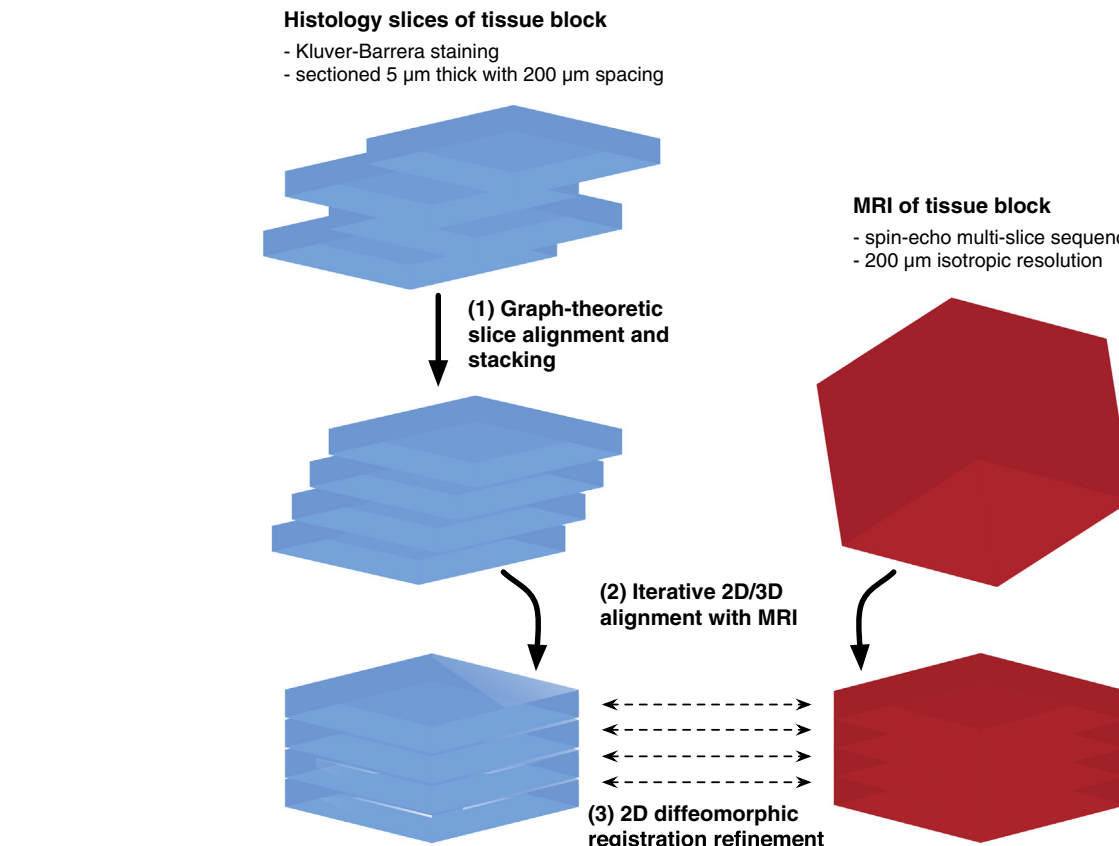


Fig. 6. Major stages of histology reconstruction pipeline shown schematically for one tissue sub-block.

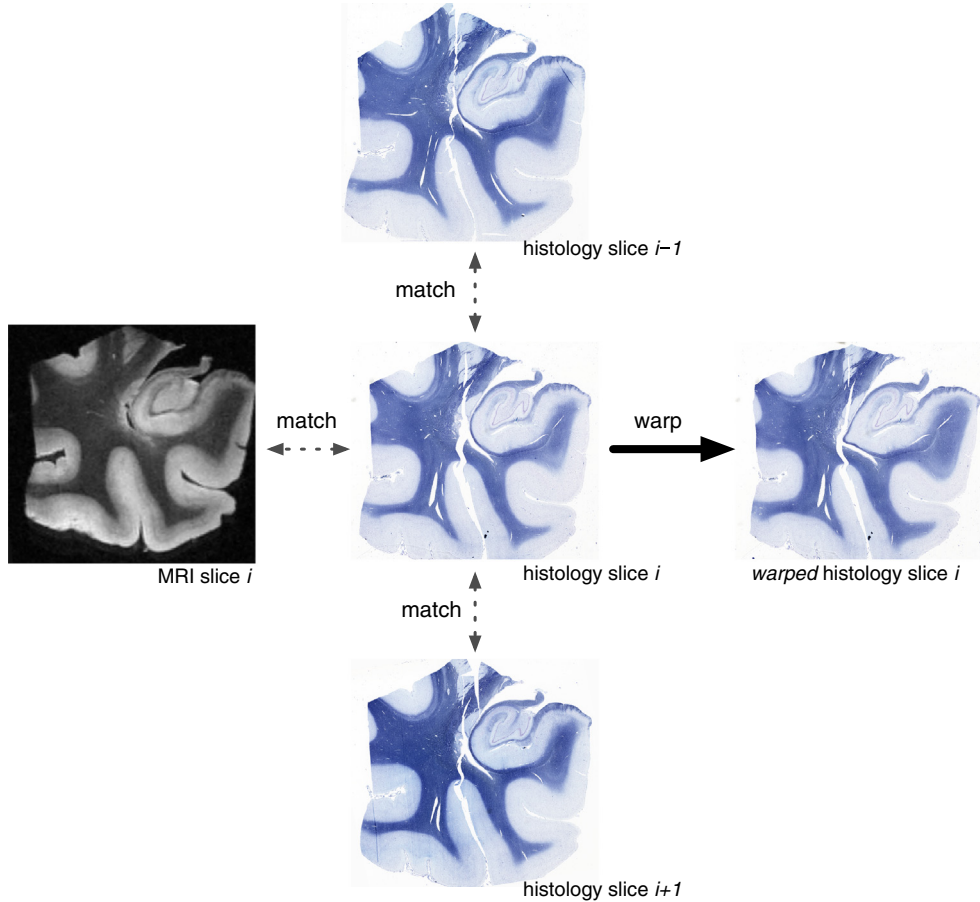


Fig. 7. Schematic of diffeomorphic registration of histology slice h_i simultaneously to its neighbors h_{i-1}, h_{i+1} , and to corresponding MRI slice m_i .

stage: Let μ_i and σ_i be the mean and standard deviation of values in N_i . We defined $a_{i,i-1} = (1 + \exp(-(NMI(h_i, h_{i-1}) - \mu_i) / \sigma_i))^{-1}$ and similarly, $a_{i,i+1} = (1 + \exp(-(NMI(h_i, h_{i+1}) - \mu_i) / \sigma_i))^{-1}$. We used a fixed weight $b = 0.75$, which favored matching histology to MRI while preserving continuity between histology slices.

After performing this registration for all slices $\{h_1, \dots, h_N\}$ of \hat{H}^0 in sequential order, the warped slices were stacked into a new volume \hat{H}^1 . We continued iterating over all slices of \hat{H}^1 in the same manner (constructing \hat{H}^2, \hat{H}^3 , etc.) until the relative change at iteration k between $NMI(\hat{H}^k, \hat{M})$ and $NMI(\hat{H}^{k+1}, \hat{M})$ fell below 0.5×10^{-5} . For the

histology sub-blocks, this led to between 21 and 25 reconstruction iterations.

Registration of tissue sub-block MRIs to whole-HF MRI

As a final step, the MRIs of the approximately 1 cm thick tissue sub-blocks were registered to the MRI of the whole HF that was acquired prior to cutting. Registrations were done in ANTs using the normalized cross-correlation metric and 9-DOF scaling transformations in order to account for global tissue shrinkage due to embedding. Since histology

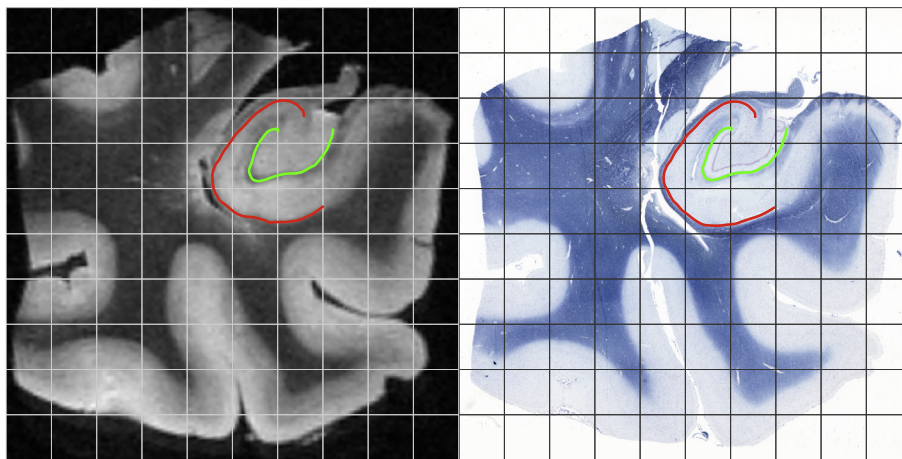


Fig. 8. Corresponding coronal MRI (left) and histology (right) sections following diffeomorphic reconstruction. Sample evaluation curves for boundary displacement error computation are shown for the cornu Ammonis (CA, red) and stratum radiatum, stratum lacunosum-moleculare, and hippocampal sulcus (SLRM-HS, green).

from each sub-block was reconstructed into the space of its respective sub-block MRI, these transformations also mapped histology to the space of the whole-HF MRI. All segmentation labels were also transferred from the original histology sections to the whole-HF MRI volume.

Subfield label refinement in whole-HF MRI space

In whole-HF MRI space, the transferred subfield labels were manually refined in ITK-SNAP (Yushkevich et al., 2006b) in order to account for residual errors in the histology-to-MRI mapping and gaps in labels due to missing or damaged tissue. The CA and SUB labels were adjusted to agree with the visible pial and white matter cortical boundaries in the coronal plane of the MRI reference. Transitions between subfield label boundaries (i.e. SUB/CA1, CA1/CA2, CA2/CA3, CA3/DG) were not modified, since they were not supported by MRI contrast and only evident in histology. The result is a smoother segmentation that better adheres to the MRI intensity features. For MRI slices that fell in between the histology stacks (i.e. slices at the edges of the tissue blocks), the delineation was extrapolated by manually extrapolating the subfield boundaries derived from neighboring histology sections.

Evaluation of reconstruction accuracy

As a measure of reconstruction accuracy, we evaluated the average displacement error of the outer CA boundary and the inner SRLM-HS boundary in both MRI and histology following the three sequential stages of reconstruction. Specifically, the first boundary separates the gray matter of CA from surrounding white matter, and it was drawn at the interface of the stratum oriens and the stratum pyramidale. The second boundary approximately separates DG from the CA subfields and SUB. In histology, it was marked as the innermost boundary of the SRLM-HS label. Both boundaries run roughly parallel to the vestigial hippocampal sulcus and reliably appear with high contrast in histology and MRI (Duvernoy, 2005; Fatterpekar et al., 2002; Malykhin et al., 2010). We demarcated the boundaries in histology and MRI prior to executing image pre-processing and the reconstruction pipeline. sample demarcations of boundary curves are shown in Fig. 8 for two corresponding MRI and histology slices following reconstruction with diffeomorphic co-registration refinement.

Boundary displacement error (BDE) was calculated between the two boundary curves in MRI and histology following the sequential stages of reconstruction: **slice stacking**, **affine 2D/3D histology-MRI co-registration refinement**, and **2D diffeomorphic co-registration refinement**. Additionally, we evaluated slice stacking both with and

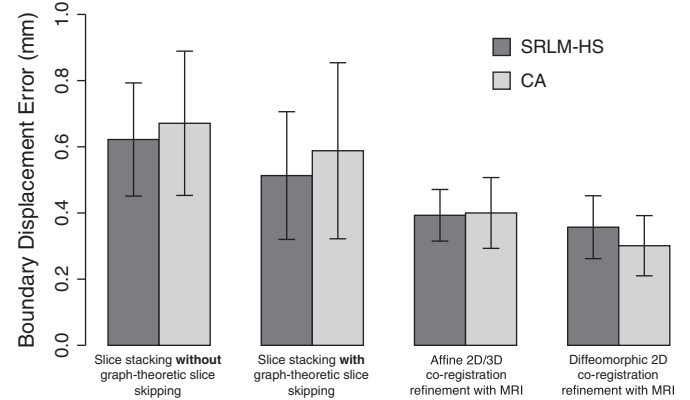


Fig. 10. Mean boundary displacement errors between stratum radiatum, lacunosum-moleculare, and hippocampal sulcus (SRLM-HS) and cornu Ammonis (CA) boundaries in reconstructed histology sub-blocks following application of sequential stages of volumetric reconstruction (error bars indicate standard deviation).

without the graph-theoretic slice skipping algorithm. The graph-theoretic algorithm was disabled by setting a registration neighborhood size of $k = 1$ and a value of $\epsilon = 0$ in Eq. (2) for edge weights. Evaluation of BDE was performed on six equally spaced slices from each tissue sub-block, in the anatomical space of the original sub-block MRIs. For two boundaries defined by point sets A and B , the BDE metric is defined as follows:

$$\text{BDE}(A, B) = \left(\frac{1}{|A|} \sum_{p \in A} d(p, B)^2 + \frac{1}{|B|} \sum_{p \in B} d(p, A)^2 \right)^{\frac{1}{2}}, \quad (5)$$

where $d(p, A)$ and $d(p, B)$ are the Euclidean distances from point p to the closest point on boundaries A and B , respectively.

Results

In this section, we present the results of histology reconstruction and the mapping of subfield labels into MRI space. Fig. 9 shows reconstructed histology from two HF tissue sub-blocks following sequential stages of the volumetric reconstruction algorithm. The first two rows demonstrate the results of slice stacking without and with graph-theoretic slice stacking, respectively. Reconstructions are also shown following affine 3D/2D

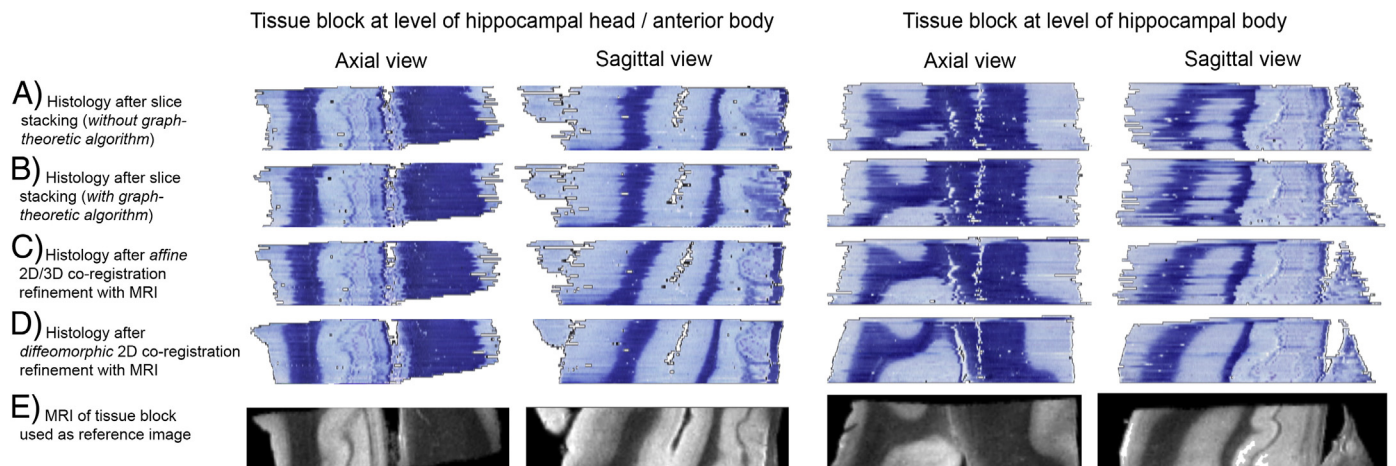


Fig. 9. Axial and sagittal views of reconstructed histology from two tissue sub-blocks following stages of reconstruction: slice stacking (A) with and (B) without graph-theoretic slice-skipping, (C) affine co-registration refinement with reference MRI, and (D) diffeomorphic co-registration refinement with reference MRI. The reference MRI of each sub-block is shown in row (E).

co-registration and diffeomorphic 2D co-registration refinement with the tissue sub-block MRI. Slices were generally aligned in the initial reconstruction, but some features (e.g. white and gray matter boundaries, tissue boundaries, and the SRLM-HS) were not continuous along the

stacking (*z*) dimension. Affine co-registration with MRI and further diffeomorphic co-registration refinement significantly improved visual reconstruction quality, as increased continuity was seen between anatomical structures along *z*. This observation is quantified in Fig. 10,

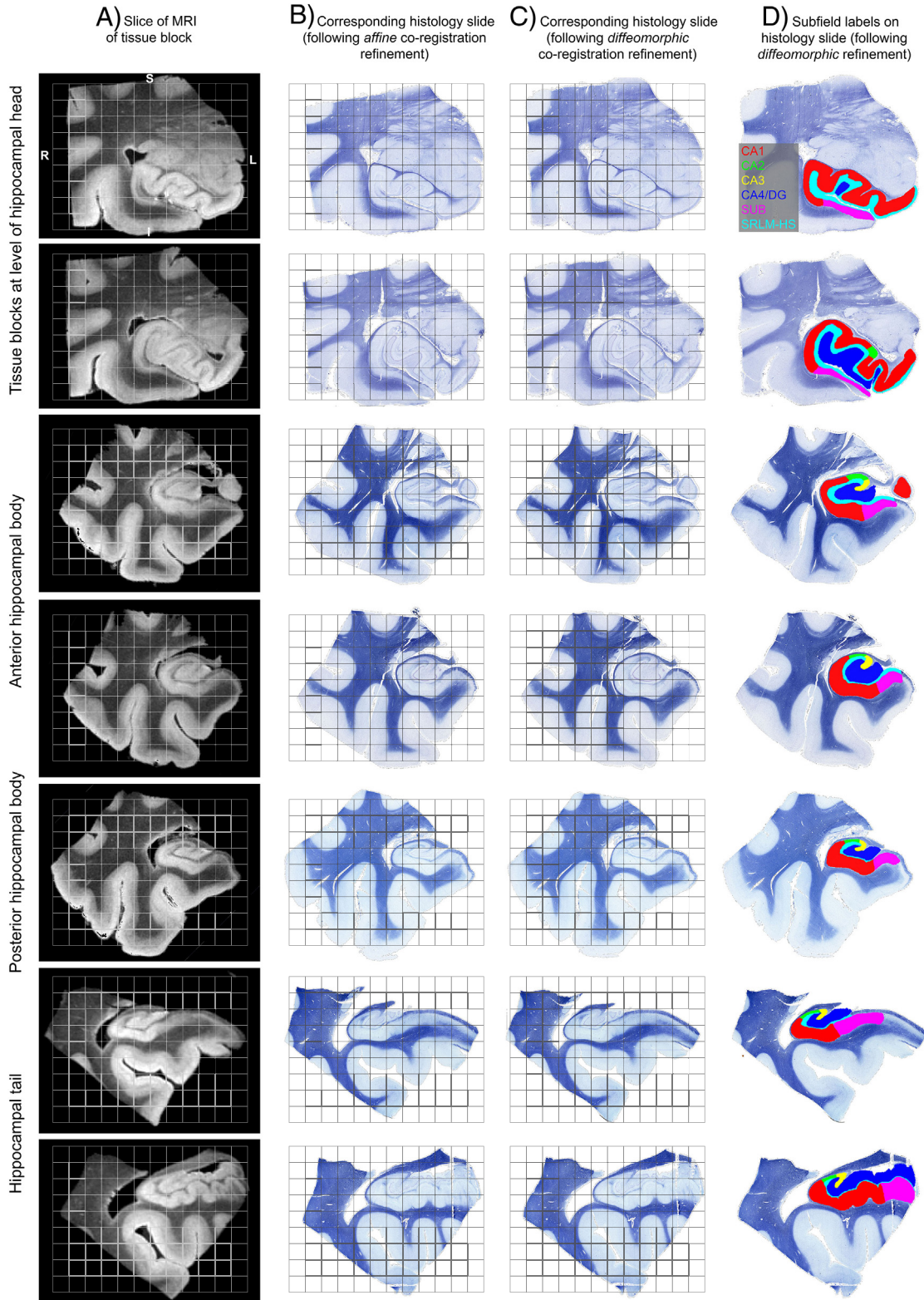


Fig. 11. Coronal slices at level of hippocampal head, body, and tail comparing (A) tissue sub-block MRI with reconstructed histology following (B) affine and (C) diffeomorphic co-registration. Subfield labels are overlaid following affine and diffeomorphic warping in column (D).

which shows that mean displacement error between corresponding anatomical boundaries in histology and MRI decreased using graph-theoretic slice stacking and following the MRI co-registration refinement steps.

While Fig. 9 highlights reconstruction results in the axial and sagittal planes, Fig. 11 shows comparisons of matching histology and MRI coronal slices following affine and diffeomorphic co-registration refinement. Representative slices are given from the hippocampal head, body, and tail of the specimen, with subfield labels shown on the warped histology. While differences are more subtle than in the axial and sagittal views, residual differences between the MRI and histology coronal slices are seen to decrease following diffeomorphic refinement between the two modalities.

To demonstrate the reconstruction of the entire sample, we show the tissue sub-blocks registered and resampled into the space of the whole-HF MRI using 3D scaling transforms. Fig. 12 shows axial and sagittal views of the whole-HF MRI, the co-registered sub-block MRIs, and the reconstructed histology following warping to the space of the whole-HF. The sixth tissue sub-block did not contain HF structures and is not shown. After registration, gaps (oriented along oblique

coronal planes) existed between the reconstructed histology and MRI sub-blocks. Despite these gaps, which were due to tissue lost or damaged at the ends of sub-blocks during cutting and microtome sectioning, the main hippocampal structures were visually well aligned between the registered sub-blocks.

The subfield segmentation labels derived from histology are shown overlaid on the whole-HF MRI in Fig. 13. Labels are shown before and after manual label refinement using the whole-HF MRI as reference. There is visually improved smoothness and consistency of label boundaries following refinement. Three-dimensional renderings of the subfield labels in whole-HF space are shown in Fig. 14, both before and after manual label correction. Fig. 15 displays the final subfield segmentation labels overlaid on MRI slices of the head, body, and tail from the whole HF. This is the same data displayed in columns (D) of Fig. 13, but shown resliced along coronal planes aligned with the anterior-posterior axis of the HF. Since the MRI and final subfield labels have 160 μm isotropic resolution, they can be resliced along arbitrary axes.

Table 3 reports volumes of the region labels in the annotated post-mortem dataset. These volumes were computed following manual label correction in the space of the MRI of the fixed, whole HF specimen.

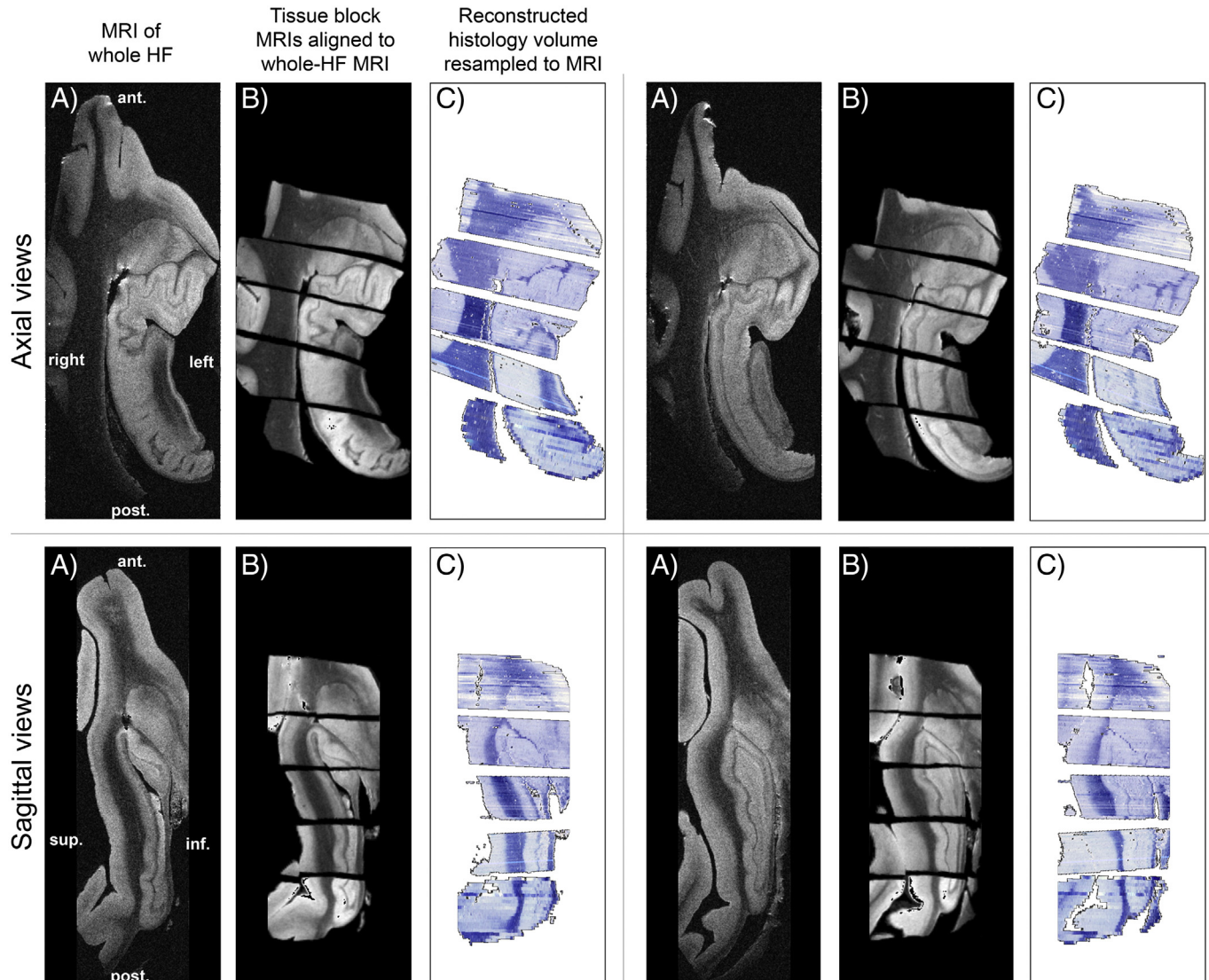


Fig. 12. Axial and sagittal views of (A) whole-HF MRI; (B) tissue sub-block MRIs co-registered to whole-HF MRI using 9-degree-of-freedom scaling transforms; and (C) reconstructed histology resampled to the whole-HF MRI.

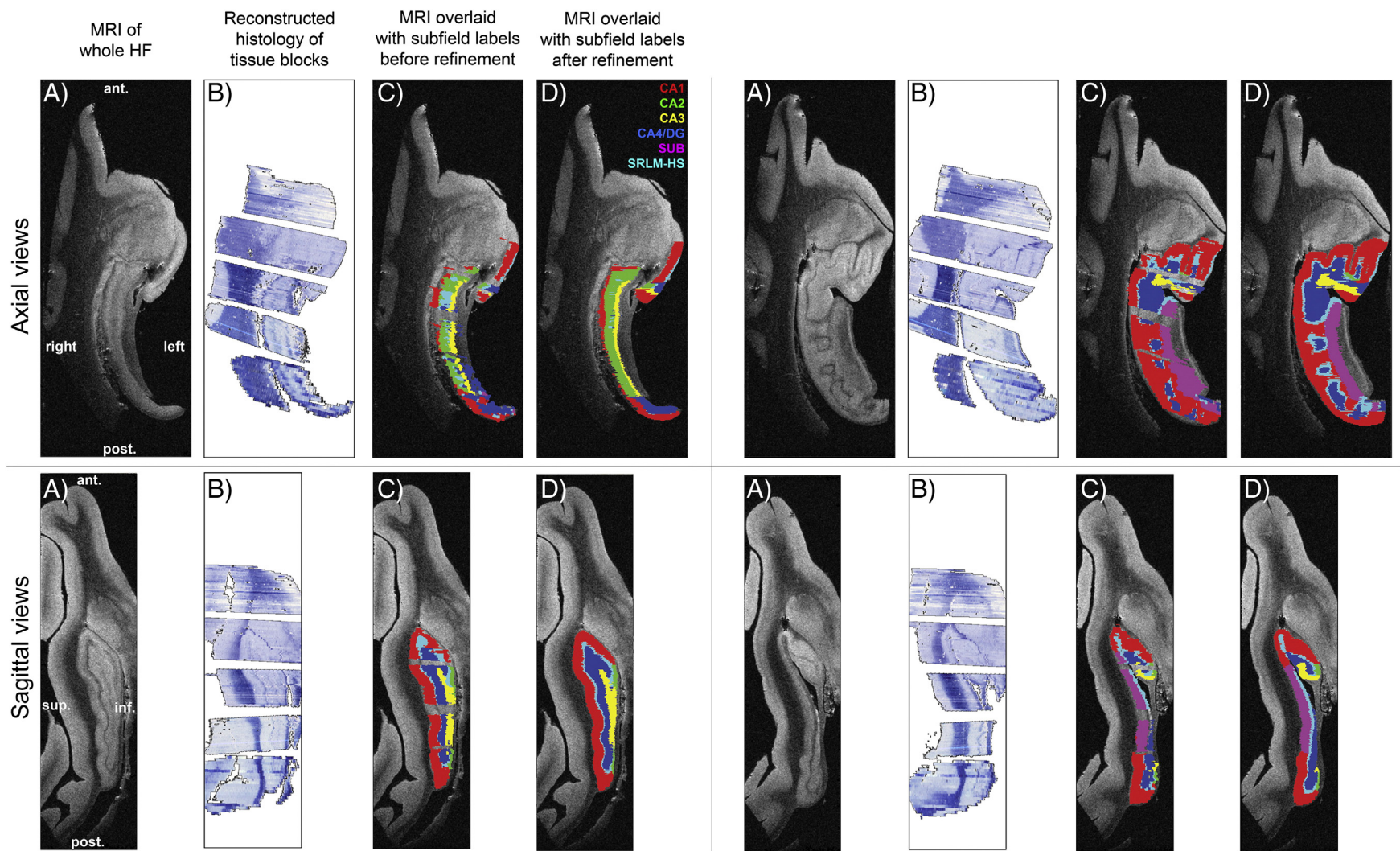


Fig. 13. Hippocampal subfield labels derived from histology shown before and after manual refinement. All images and labels are in the anatomical space of the whole-HF MRI: (A) whole-HF MRI; (B) final reconstructed histology; and whole-HF MRI overlaid with subfield labels (C) before and (D) after manual refinement.

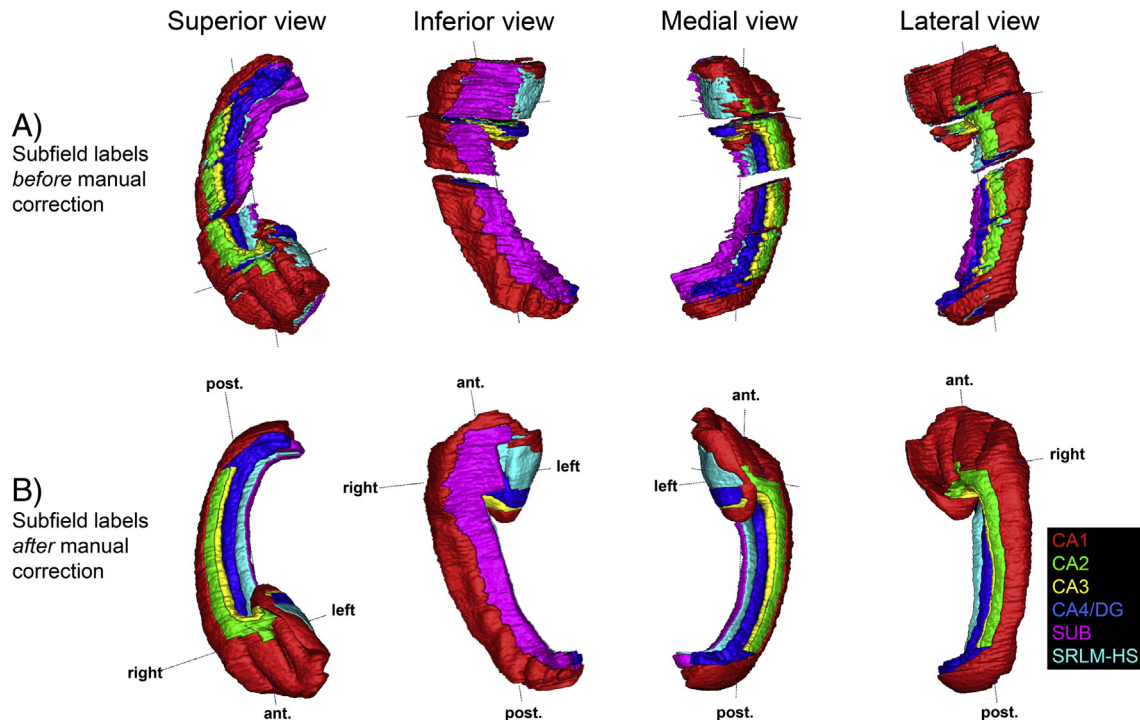


Fig. 14. Hippocampal subfield labels derived from histology reconstructed in 3D (A) before and (B) after manual label refinement.

Discussion

The primary contribution of this work is a detailed, three-dimensional reconstruction of the human hippocampal formation from histology and high-resolution, postmortem MRI of the same specimen. Hippocampal subfield labels are derived from reconstructed histology in which the subfields were manually segmented based on cellular features. MRI of the whole HF serves as the anatomical reference space for reconstruction and for the final labels. To our knowledge, this is the first time that a high-resolution MRI dataset of the whole human HF has been parcellated into subfields based on cytoarchitectonic features mapped directly from histological imaging.

The mapping of anatomical labels from histological space into 3D postmortem MRI space is a necessary technical step for building a comprehensive atlas of the hippocampal formation from multiple samples that relates MRI appearance to cytoarchitecture. Performing this reconstruction pipeline on multiple samples, which will form part of future work, will allow the atlas to describe the anatomical variability in the distribution of hippocampal subfields relative to the variability in overall hippocampal shape and in MRI appearance. Such a resource would describe how the location of subfield boundaries unseen in MRI varies relative to structures and boundaries that can be seen in MRI. The present paper, together with our earlier MRI-only paper (Yushkevich et al., 2009), which presents the feasibility of combining postmortem MRI scans into a probabilistic atlas, form building blocks toward our ultimate goal of building the comprehensive atlas.

To ensure that the mapping of anatomical boundaries from histology space to MRI space was accurate, we evaluated the mean displacement error between two anatomical boundaries that can be reliably labeled in both modalities: the outer boundary of CA gray matter and the innermost boundary of the SRLM-HS. As expected, sequential stages of the histology reconstruction pipeline, from histology slice stacking through affine and diffeomorphic co-registration refinement with MRI, led to successive reduction in the boundary displacement error, as shown in Figs. 9 and 10. As Figs. 11 and 12 show, the matching of other anatomical

features between the two modalities is also largely visually consistent. The largest apparent anatomical differences between the modalities are observed in ventricular spaces and at section peripheries due to large physical deformations that most likely took place during tissue embedding and sectioning.

The final mean boundary displacement error in the quantitative evaluation is on the order of 0.5 mm. While this error is not insignificant in comparison to the thickness of hippocampal strata, it is relatively small in contrast to the uncertainty of the location of the boundaries between hippocampal subfields along the strata, which are not hard boundaries, but rather soft transition zones. Compared to the degree of variability in the definition of hippocampal subfields in MRI literature, illustrated in Fig. 1, errors on the order of 0.5 mm introduced by the histology to MRI mapping can be considered relatively small.

Application of the manual correction to histological labels in MRI space, illustrated in Figs. 13 and 14, allows errors in the direction across hippocampal strata to be rectified, since the relevant boundaries (between CA gray matter and surrounding white matter, and between CA and DG) are well defined in MRI space. By performing manual segmentation in histology space, then applying corrections in MRI space, we are able to bring into the MRI space the relevant cytoarchitectonic information that is not present there, without having to compromise the quality of boundaries between hippocampal strata that can be observed in MRI directly. In addition, manual post-processing in MRI space allowed subfield boundaries to be extrapolated to regions of the MRI that were left unsegmented due to unrecoverable tissue loss at the ends of sub-blocks. However, this procedure assumed a degree of visual continuity between subfields across slices.

In Table 3, we report labeled region volumes (following tissue fixation) in the whole-HF MRI dataset. The volumes that we report for CA1, CA2–3 (combined), and DG are comparable in magnitude to volumes estimated in postmortem histology studies by West and Gundersen (1990) and Simic et al. (1997). However, we emphasize that our volumes are based on a single subject. Furthermore, the volumes in our study are estimated directly in the 3D MRI space, whereas

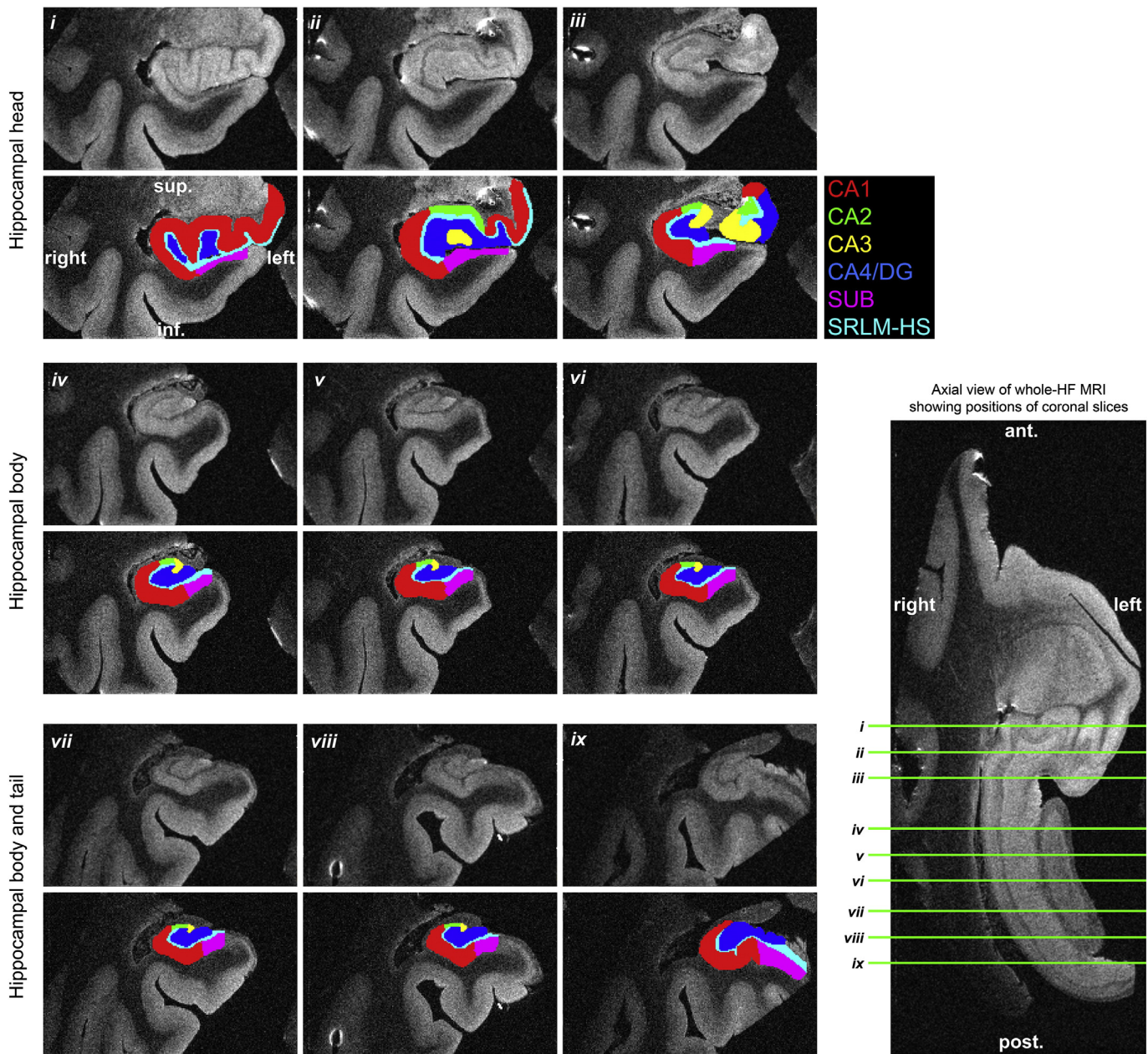


Fig. 15. Coronal slices of whole-HF MRI overlaid with final subfield labels derived from histology following volumetric reconstruction. Slice positions are depicted on an axial section of whole-HF MRI.

the studies by West and Gundersen (1990) and Simic et al. (1997) estimated volumes from a small number of sections (~10) along the length of the hippocampus, necessitating correction for tissue shrinkage in histological processing.

Table 3
Region volumes of HF in segmented whole-HF MRI dataset

Region	Volume (mm ³)
CA1	1188.7
CA2	65.6
CA3	87.2
DG	451.4
SUB	282.8
SRLM-HS	285.8
Total	2361.6

There is room for improvement in our current MRI and histology acquisition pipelines. For instance, using smaller coils and tissue samples processed with contrast agent, Fischl et al. (2009) and Augustinack et al. (2010) obtained scans of the whole HF at resolution as high as 0.1 mm isotropic, which revealed even greater detail. In our future work, MRI samples obtained with a smaller 35 mm radiofrequency coil will be used, which will improve contrast and resolution. However, even at this higher resolution, MRI fails to provide features necessary to define most subfield boundaries. Additionally, incorporating block-face imaging into the histology acquisition pipeline could be used to more directly guide reconstruction or to facilitate correction of slice distortions, such as tears or debris, without reference to MRI (Dauguet et al., 2007a; Yelnik et al., 2007).

The premise of accurate labeling of subfields in postmortem MRI in this study rests on both accurate segmentation and reconstruction of the histology. Our segmentations were based on cytoarchitectural features and information presented in a published atlas of the human HF.

Even at this level of detail, disagreements are likely to arise between researchers on where subfield boundaries should be placed, particularly in the anterior and posterior hippocampal regions. In fact, one of the limitations of the current study is that the manual segmentation was not done by a professional neuroanatomist and may have errors, particularly in the more complex transition zones, such as SUB/CA1 and those in the anterior hippocampus. We note, however, that the reconstruction strategy that we presented can be used with any manual labeling of the histology data, and can be corrected or adjusted in future work. On the other hand, discrete transitions between labels may not be best suited to representing subfield boundaries. Transitions between subfields encompass zones of intermediate cell shapes and densities that may be more appropriately represented by fuzzy subfield label boundaries in a future atlas. Furthermore, the reconstruction pipeline, if coupled with techniques for automated feature extraction from histology, can allow the mapping of cytoarchitectonic features themselves into the MRI space. Correlating these features with macroscopic changes derived from MRI analysis may lead to more relevant inferences than the current approach of integrating these macroscopic changes over discrete subfield labels.

A further limitation of the present work is that it captures the anatomy of a single, fixed specimen. We must therefore exercise caution in using it to derive inferences on subfield distribution. In earlier work, which did not incorporate histology, we developed and evaluated tools for combining postmortem MRI scans of multiple individuals to form a probabilistic atlas of the HF (Yushkevich et al., 2009).

We foresee several applications of this work and a future probabilistic atlas that could have significant impact in neuroimaging of the HF. The ability to relate cytoarchitectonic information and MRI appearance throughout the HF and at any cross-section makes this a significantly richer resource than printed atlases (Amaral and Lavenex, 2007; Duvernoy, 2005; Mai and Paxinos, 2011) for guiding the development of more valid manual segmentation protocols for *in vivo* MRI. Whereas multiple such segmentation protocols have been proposed in the literature, the rules that they use to define subfield boundaries are sometimes strikingly different, as Fig. 1 illustrates. This discrepancy in what different authors label as subfields can compromise the ability to compare the results of different studies, which limits the utility of subfield measurements in many applications. Characterizing the relationships between the histological and MRI appearance of the subfields has the potential to quantify the anatomical validity of the heuristic rules currently used for subfield delineation in MRI studies. Although there has been a concerted effort to harmonize the segmentation protocol for the whole hippocampus in T1-weighted MRI (Boccardi et al., 2011; Frisoni and Jack, 2011; Jack et al., 2011), such a task is yet to be performed for hippocampal subfields. By linking MRI appearance to microscopic features, our reconstruction can potentially serve as a useful reference dataset for the eventual harmonization effort. Furthermore, given the recent success of automated techniques at propagating manual subfield segmentations from a set of training data to new unlabeled images (Pluta et al., 2012; Van Leemput et al., 2009), our work may have impact on the anatomical accuracy of automated HF segmentation algorithms developed in the future. Lastly, a future probabilistic atlas will have the potential to serve as a reference space for the HF, into which functional data from *in vivo* functional MRI studies can be brought in by means of shape-based normalization (Das et al., 2011; Kirwan et al., 2007) and analyzed in the context of hippocampal substructure.

Funding

This work was supported by National Institutes of Health grants [R01-AG037376, K25-AG027785, K25-AG027785-03S1]; a Natural Sciences and Engineering Research Council of Canada (NSERC) Canada Graduate Scholarship to D.H.A.; and the University of Pennsylvania's Howard Hughes Medical Institute (HHMI) Interfaces program to D.H.A.

Acknowledgments

We acknowledge the assistance of Alex Yang Liu, Gang Song, Sylvia Orozco, Stephen Pickup, Ph.D., Weixia Liu, Ph.D., and Murat Altinay, M.D. We also acknowledge the National Human Tissue Resource Center of the National Disease Research Interchange (Philadelphia, PA) for providing the tissue samples for this research. We are grateful to Prof. John Q. Trojanowski, M.D., Ph.D., Prof. Murray Grossman, M.D., Ed.D., and Prof. David A. Wolk, M.D. for their support of this work and their invaluable input.

Appendix A. Supplementary data

Supplementary data to this article can be found online at <http://dx.doi.org/10.1016/j.neuroimage.2013.08.067>.

References

- Amaral, D., Lavenex, P., 2007. *The Hippocampus Book*. Oxford University Press, Cambridge.
- Amunts, K., Kedo, O., Kindler, M., Pieperhoff, P., Mohlberg, H., Shah, N., Habel, U., Schneider, F., Zilles, K., 2005. Cytoarchitectonic mapping of the human amygdala, hippocampal region and entorhinal cortex: intersubject variability and probability maps. *Anat. Embryol.* 210 (5–6), 343–352.
- Amunts, K., Lepage, C., Borgeat, L., Mohlberg, H., Dickscheid, T., Rousseau, M.-T., Bludau, S., Bazin, P.-L., Lewis, L.B., Oros-Peusquens, A.-M., 2013. BigBrain: an ultrahigh-resolution 3D human brain model. *Science* 340 (6139), 14721475.
- Apostolova, L.G., Dinov, I.D., Dutton, R.A., Hayashi, K.M., Toga, A.W., Cummings, J.L., Thompson, P.M., 2006. 3D comparison of hippocampal atrophy in amnestic mild cognitive impairment and Alzheimer's disease. *Brain* 129 (11), 2867–2873.
- Arganda-Carreras, I., Sorzano, C.O.S., Thévenaz, P., Muñoz, Barrutia A., Kybic, J., Marabini, R., Carazo, J.M., Ortiz-de, Solorzano C., 2010. Non-rigid consistent registration of 2D image sequences. *Phys. Med. Biol.* 55 (20), 6215–6242.
- Augustinack, J.C., Helmer, K., Huber, K.E., Kakunoori, S., Zöllei, L., Fischl, B., 2010. Direct visualization of the perforant pathway in the human brain with ex vivo diffusion tensor imaging. *Front. Hum. Neurosci.* 4 (42), 1–13.
- Avants, B., Epstein, C., Grossman, M., Gee, J., 2008. Symmetric diffeomorphic image registration with cross-correlation: evaluating automated labeling of elderly and neurodegenerative brain. *Med. Image Anal.* 12 (1), 26–41.
- Avants, B., Tustison, N., Wu, J., Cook, P., Gee, J., 2011. An Open Source Multivariate Framework for n-Tissue Segmentation with Evaluation on Public Data. University of Pennsylvania Image Computing and Science Laboratory (Whitepaper).
- Bakker, A., Kirwan, C.B., Miller, M., Stark, C.E.L., 2008. Pattern separation in the human hippocampal CA3 and dentate gyrus. *Science* 319 (5870), 1640–1642.
- Bardinet, E., Bhattacharjee, M., Dormont, D., Pidoux, B., Malandaïn, G., Schpbach, M., Ayache, N., Cornu, P., Agid, Y., Yelnik, J., 2009. A three-dimensional histological atlas of the human basal ganglia. II. Atlas deformation strategy and evaluation in deep brain stimulation for Parkinson disease. *J. Neurosurg.* 110 (2), 208–219.
- Barnes, J., Bartlett, J.W., van de Pol, L.A., Loy, C.T., Scialli, R.I., Frost, C., Thompson, P., Fox, N.C., 2009. A meta-analysis of hippocampal atrophy rates in Alzheimer's disease. *Neurobiol. Aging* 30 (11), 1711–1723.
- Beare, R., Richards, K., Murphy, S., Petrou, S., Reutens, D., 2008. An assessment of methods for aligning two-dimensional microscope sections to create image volumes. *J. Neurosci. Methods* 170 (2), 332–344.
- Bird, C.M., Burgess, N., 2008. The hippocampus and memory: insights from spatial processing. *Nat. Rev. Neurosci.* 9 (3), 182–194.
- Blamire, A.M., Rowe, J.G., Styles, P., McDonald, B., 1999. Optimising imaging parameters for post mortem MR imaging of the human brain. *Acta Radiol.* 40 (6), 593–597.
- Bobinski, M., de Leon, M.J., Tarnawski, M., Wegiel, J., Bobinski, M., Reisberg, B., Miller, D.C., Wisniewski, H.M., 1998. Neuronal and volume loss in CA1 of the hippocampal formation uniquely predicts duration and severity of Alzheimer disease. *Brain Res.* 805 (1), 267–269.
- Boccardi, M., Ganzola, R., Bocchetta, M., Pievani, M., Redolfi, A., Bartzokis, G., Camicioli, R., Csernansky, J.G., de Leon, M.J., deToledo-Morrell, L., 2011. Survey of protocols for the manual segmentation of the hippocampus: preparatory steps towards a joint EADC–ADNI harmonized protocol. *J. Alzheimers Dis.* 26, 61–75.
- Bonnici, H.M., Chadwick, M.J., Kumaran, D., Hassabis, D., Weiskopf, N., Maguire, E.A., 2012. Multi-voxel pattern analysis in human hippocampal subfields. *Front. Hum. Neurosci.* 6.
- Braak, H., Braak, E., 1991. Neuropathological stageing of Alzheimer-related changes. *Acta Neuropathol.* 82 (4), 239–259.
- Braak, H., Alafuzoff, I., Arzberger, T., Kretzschmar, H., Tredici, K., 2006. Staging of Alzheimer disease-associated neurofibrillary pathology using paraffin sections and immunocytochemistry. *Acta Neuropathol.* 112 (4), 389–404.
- Breen, M.S., Lancaster, T.L., Wilson, D.L., 2005a. Correcting spatial distortion in histological images. *Comput. Med. Imaging Graph.* 29 (6), 405–417.
- Breen, M.S., Lazebnik, R.S., Wilson, D.L., 2005b. Three-dimensional registration of magnetic resonance image data to histological sections with model-based evaluation. *Ann. Biomed. Eng.* 33 (8), 1100–1112.
- Bürgel, U., Schormann, T., Schleicher, A., Zilles, K., 1999. Mapping of histologically identified long fiber tracts in human cerebral hemispheres to the MRI volume of a reference brain: position and spatial variability of the optic radiation. *NeuroImage* 10 (5), 489–499.

- Burgess, N., Maguire, E.A., O'Keefe, J., 2002. The human hippocampus and spatial and episodic memory. *Neuron* 35 (4), 625–642.
- Cannestra, A.F., Santori, E.M., Holmes, C.J., Toga, A.W., 1997. A three-dimensional multimodality brain map of the nemestrina monkey. *Brain Res. Bull.* 43 (2), 141–148.
- Ceritoglu, C., Wang, L., Selement, L.D., Csernansky, J.G., Miller, M.I., Ratnanather, J.T., 2010. Large deformation diffeomorphic metric mapping registration of reconstructed 3D histological section images and in vivo MR images. *Front. Hum. Neurosci.* 4.
- Chakeres, D.W., Whitaker, C.D., Dashner, R.A., Scharre, D.W., Beversdorf, D.Q., Raychaudhury, A., Schmalbrock, P., 2005. High-resolution 8 Tesla imaging of the formalin-fixed normal human hippocampus. *Clin. Anat.* 18 (2), 88–91.
- Chakravarty, M.M., Bertrand, G., Hodge, C.P., Sadikot, A.F., Collins, D.L., 2006. The creation of a brain atlas for image guided neurosurgery using serial histological data. *Neuroimage* 30 (2), 359–376.
- Choe, A.S., Gao, Y., Li, X., Compton, K.B., Stepniewska, I., Anderson, A.W., 2011. Accuracy of image registration between MRI and light microscopy in the ex vivo brain. *Magn. Reson. Imaging* 29 (5), 683–692.
- Cifor, A., Pridmore, T., Pitiot, A., 2009. Smooth 3-D reconstruction for 2-D histological images. *Lect. Notes Comput. Sci* 5636, 350–361.
- Das, S.R., Mechanic-Hamilton, D., Pluta, J., Korczykowski, M., Detre, J.A., Yushkevich, P.A., 2011. Heterogeneity of functional activation during memory encoding across hippocampal subfields in temporal lobe epilepsy. *Neuroimage* 58 (4), 1121–1130.
- Dauguet, J., Delzescaux, T., Cond, F., Mangin, J.F., Ayache, N., Hantraye, P., Frouin, V., 2007a. Three-dimensional reconstruction of stained histological slices and 3D non-linear registration with in-vivo MRI for whole baboon brain. *J. Neurosci. Methods* 164 (1), 191–204.
- Dauguet, J., Peled, S., Berezovskii, V., Delzescaux, T., Warfield, S.K., Born, R., Westin, C.F., 2007b. Comparison of fiber tracts derived from in-vivo DTI tractography with 3D histological neural tract tracer reconstruction on a macaque brain. *Neuroimage* 37 (2), 530–538.
- Dawie, R.J., Bennett, D.A., Schneider, J.A., Vasireddi, S.K., Arfanakis, K., 2009. Postmortem MRI of human brain hemispheres: T2 relaxation times during formaldehyde fixation. *Magn. Reson. Med.* 61 (4), 810–818.
- Duvernoy, H., 2005. The Human Hippocampus: Functional Anatomy, Vascularization and Serial Sections with MRI. Springer.
- Ekstrom, A.D., Bazil, A.J., Suthana, N.A., Al-Hakim, R., Ogura, K., Zeineh, M., Burggren, A.C., Bookheimer, S.Y., 2009. Advances in high-resolution imaging and computational unfolding of the human hippocampus. *Neuroimage* 47 (1), 42–49.
- Fanselow, M.S., Dong, H.-W., 2010. Are the dorsal and ventral hippocampus functionally distinct structures? *Neuron* 65 (1), 7–19.
- Fatterpekar, G.M., Naidich, T.P., Delman, B.N., Aguinaldo, J.G., Gultekin, S.H., Sherwood, C.C., Hof, P.R., Drayer, B.P., Fayad, Z.A., 2002. Cytoarchitecture of the human cerebral cortex: MR microscopy of excised specimens at 9.4 Tesla. *Am. J. Neuroradiol.* 23 (8), 1313–1321.
- Feuerstein, M., Heibel, H., Gardazabal, J., Navab, N., Groher, M., 2011. Reconstruction of 3-D histology images by simultaneous deformable registration. *Med. Image Comput. Comput. Assist. Interv.* 14 (2), 582–589.
- Fischl, B., Stevens, A.A., Rajendran, N., Yeo, B.T., Greve, D.N., Van Leemput, K., Polimeni, J.R., Kakunoori, S., Buckner, R.L., Pacheco, J., Salat, D.H., Melcher, J., Frosch, M.P., Hyman, B.T., Grant, P.E., Rosen, B.R., van der Kouwe, A.J., Wiggins, G.C., Wald, L.L., Augustinack, J.C., 2009. Predicting the location of entorhinal cortex from MRI. *Neuroimage* 47 (1), 8–17.
- Frisoni, G.B., Jack, C.R., 2011. Harmonization of magnetic resonance-based manual hippocampal segmentation: a mandatory step for wide clinical use. *Alzheimers Dement.* 7 (2), 171–174.
- Gefen, S., Tretiak, O., Nissanov, J., 2003. Elastic 3-D alignment of rat brain histological images. *IEEE Trans. Med. Imaging* 22 (11), 1480–1489.
- Geuze, E., Vermetten, E., Bremner, J.D., 2004. MR-based in vivo hippocampal volumetrics: 2. Findings in neuropsychiatric disorders. *Mol. Psychiatry* 10 (2), 160–184.
- Gómez-Isla, T., Price, J.L., McKeel Jr., D.W., Morris, J.C., Growdon, J.H., Hyman, B.T., 1996. Profound loss of layer II entorhinal cortex neurons occurs in very mild Alzheimer's disease. *J. Neurosci.* 16 (14), 4491–4500.
- Groen, H.C., van Walsum, T., Rozie, S., Klein, S., van Gaalen, K., Gijsen, F.J.H., Wielopolski, P.A., van Beusekom, H.M.M., de Crom, R., Verhagen, H.J.M., 2010. Three-dimensional registration of histology of human atherosclerotic carotid plaques to in-vivo imaging. *J. Biomech.* 43 (11), 2087–2092.
- Guest, E., Baldock, R., 1995. Automatic reconstruction of serial sections using the finite element method. *Bioimaging* 3 (4), 154–167.
- Hanseeuw, B.J., Van Leemput, K., Kavec, M., Grandin, C., Seron, X., Ivanoiu, A., 2011. Mild cognitive impairment: differential atrophy in the hippocampal subfields. *Am. J. Neuroradiol.* 32 (9), 1658–1661.
- Harding, A., Halliday, G., Kril, J., 1998. Variation in hippocampal neuron number with age and brain volume. *Cereb. Cortex* 8 (8), 710–718.
- Henry, T.R., Chupin, M., Lehéricy, S., Strupp, J.P., Sikora, M.A., Zhiyi, Y.S., Ugurbil, K., Van de Moortele, P.F., 2011. Hippocampal sclerosis in temporal lobe epilepsy: findings at 7 T. *Radiology* 261 (1), 199–209.
- Hess, A., Lohmann, K., Gundelfinger, E.D., Scheich, H., 1998. A new method for reliable and efficient reconstruction of 3-dimensional images from autoradiographs of brain sections. *J. Neurosci. Methods* 84 (1), 77–86.
- Jack, C.R., Barkhof, F., Bernstein, M.A., Cantillon, M., Cole, P.E., DeCarli, C., Dubois, B., Duchesne, S., Fox, N.C., Frisoni, G.B., Hampel, H., Hill, D.L., Johnson, K., Mangin, J.-F., Scheltens, P., Schwarz, A.J., Sperling, R., Suhy, J., Thompson, P.M., Weiner, M., Foster, N.L., 2011. Steps to standardization and validation of hippocampal volumetry as a biomarker in clinical trials and diagnostic criterion for Alzheimer's disease. *Alzheimers Dement.* 7 (4), 474–485 (e.e4).
- Ju, T., Warren, J., Carson, J., Bello, M., Kakadiaris, I., Chiu, W., Thaller, C., Eichele, G., 2006. 3D volume reconstruction of a mouse brain from histological sections using warp filtering. *J. Neurosci. Methods* 156 (1), 84–100.
- Kirwan, C.B., Jones, C.K., Miller, M.I., Stark, C.E., 2007. High-resolution fMRI investigation of the medial temporal lobe. *Hum. Brain Mapp.* 28 (10), 959–966.
- Kluver, H., Barrera, E., 1953. A method for the combined staining of cells and fibers in the nervous system. *J. Neuropathol. Exp. Neurol.* 12 (4), 400–403.
- Krauth, A., Blanc, R., Poveda, A., Jeanmonod, D., Morel, A., Székely, G., 2010. A mean three-dimensional atlas of the human thalamus: generation from multiple histological data. *Neuroimage* 49 (3), 2053–2062.
- Krinidis, S., Nikou, C., Pitas, I., 2003. Reconstruction of serially acquired slices using physics-based modeling. *IEEE Trans. Inf. Technol. Biomed.* 7 (4), 394–403.
- La Joie, R., Fouquet, M., Mézenge, F., Landeau, B., Villain, N., Mevel, K., Pélerin, A., Eustache, F., Desgranges, B., Chételat, G., 2010. Differential effect of age on hippocampal subfields assessed using a new high-resolution 3 T MR sequence. *Neuroimage* 53 (2), 506–514.
- Lebenberg, J., Hérad, A.S., Dubois, A., Dauguet, J., Frouin, V., Dhenain, M., Hantraye, P., Delzescaux, T., 2010. Validation of MRI-based 3D digital atlas registration with histological and autoradiographic volumes: an anatomofunctional transgenic mouse brain imaging study. *Neuroimage* 51 (3), 1037.
- Lein, E.S., Hawrylycz, M.J., Ao, N., Ayres, M., Bensinger, A., Bernard, A., Boe, A.F., Boguski, M.S., Brockway, K.S., Byrnes, E.J., et al., 2006. Genome-wide atlas of gene expression in the adult mouse brain. *Nature* 445 (7124), 168–176.
- Leutgeb, J.K., Leutgeb, S., Moser, M.B., Moser, E.I., 2007. Pattern separation in the dentate gyrus and CA3 of the hippocampus. *Science* 315 (5814), 961–966.
- Li, X., Yankelev, T.E., Rosen, G.D., Gore, J.C., Dawant, B.M., 2009. Enhancement of histological volumes through averaging and their use for the analysis of magnetic resonance images. *Magn. Reson. Imaging* 27 (3), 401–416.
- Lisman, J.E., Otmakhova, N.A., 2001. Storage, recall, and novelty detection of sequences by the hippocampus: elaborating on the SOCRATIC model to account for normal and aberrant effects of dopamine. *Hippocampus* 11 (5), 551–568.
- Lorente de Nò, R., 1934. Studies on the structure of the cerebral cortex. II. Continuation of the study of the ammonic system. *J. Psychol. Neurol.* 46, 113–177.
- MacKenzie-Graham, A., Lee, E.F., Dinov, I.D., Bota, M., Shattuck, D.W., Ruffins, S., Yuan, H., Konstantinidis, F., Pitiot, A., Ding, Y., 2004. A multimodal, multidimensional atlas of the C57BL/6J mouse brain. *J. Anat.* 204 (2), 93–102.
- Mai, J.K., Paxinos, G., 2011. The Human Nervous System. Academic Press.
- Malandain, G., Bardinet, E., Nelissen, K., Vanduffel, W., 2004. Fusion of autoradiographs with an MR volume using 2-D and 3-D linear transformations. *Neuroimage* 23 (1), 111–127.
- Malykhin, N., Lebel, R., Coupland, N., Wilman, A., Carter, R., 2010. In vivo quantification of hippocampal subfields using 4.7 T fast spin echo imaging. *Neuroimage* 49 (2), 1224–1230.
- McLaren, D.G., Kosmatka, K.J., Oakes, T.R., Kroenke, C.D., Kohama, S.G., Matochik, J.A., Ingram, D.K., Johnson, S.C., 2009. A population-average MRI-based atlas collection of the rhesus macaque. *Neuroimage* 45 (1), 52–59.
- Meyer, C.R., Moffat, B.A., Kuszpit, K., Bland, P.L., Chenevert, T.L., Rehemtulla, A., Ross, B.D., 2006. A methodology for registration of a histological slide and in vivo MRI volume based on optimizing mutual information. *Mol. Imaging* 5 (1), 16.
- Milner, B., Johnsrude, I., Crane, J., 1997. Right medial temporal-lobe contribution to object-location memory. *Philos. Trans. R. Soc. B* 352 (1360), 1469–1474.
- Mueller, S.G., Weiner, M.W., 2009. Selective effect of age, apo e4, and Alzheimer's disease on hippocampal subfields. *Hippocampus* 19 (6), 558–564.
- Mueller, S., Stables, L., Du, A., Schuff, N., Truran, D., Cashdollar, N., Weiner, M., 2007. Measurement of hippocampal subfields and age-related changes with high resolution MRI at 4 T. *Neurobiol. Aging* 28 (5), 719–726.
- Newman, J.D., Kenkel, W.M., Aronoff, E.C., Bock, N.A., Zametkin, M.R., Silva, A.C., 2009. A combined histological and MRI brain atlas of the common marmoset monkey, *Callithrix jacchus*. *Brain Res. Rev.* 62 (1), 1–18.
- Nikou, C., Heitz, F., Nehlig, A., Namer, I.J., Armspach, J.P., 2003. A robust statistics-based global energy function for the alignment of serially acquired autoradiographic sections. *J. Neurosci. Methods* 124 (1), 93–102.
- Nunn, J.A., Graydon, F.J.X., Polkey, C.E., Morris, R.G., 1999. Differential spatial memory impairment after right temporal lobectomy demonstrated using temporal titration. *Brain* 122 (1), 47–59.
- Ourselin, S., Bardinet, E., Dormont, D., Malandain, G., Roche, A., Ayache, N., Tande, D., Parain, K., Yelnik, J., 2001a. Fusion of histological sections and MR images: towards the construction of an atlas of the human basal ganglia. *Lect. Notes Comput. Sci.* 2208, 743–751.
- Ourselin, S., Roche, A., Subsol, G., Pennec, X., Ayache, N., 2001b. Reconstructing a 3D structure from serial histological sections. *Image Vision Comput.* 19 (1), 25–31.
- Park, H., Pier, M.R., Khan, A., Shah, R., Hussain, H., Siddiqui, J., Meyer, C.R., 2008. Registration methodology for histological sections and in-vivo imaging of human prostate. *Acad. Radiol.* 15 (8), 1027.
- Pfefferbaum, A., Sullivan, E.V., Adalsteinsson, E., Garrick, T., Harper, C., 2004. Postmortem MR imaging of formalin-fixed human brain. *Neuroimage* 21 (4), 1585–1595.
- Pitiot, A., Bardinet, E., Thompson, P., Malandain, G., 2006. Piecewise affine registration of biological images for volume reconstruction. *Med. Image Anal.* 10 (3), 465–483.
- Pluta, J., Yushkevich, P., Das, S., Wolk, D., 2012. In vivo analysis of hippocampal subfield atrophy in mild cognitive impairment via semi-automatic segmentation of T2-weighted MRI. *J. Alzheimers Dis.* 31 (1), 85–99.
- Poppenk, J., Moscovitch, M., 2011. A hippocampal marker of recollection memory ability among healthy young adults: contributions of posterior and anterior segments. *Neuron* 72 (6), 931–937.
- Price, J.L., Ko, A.I., Wade, M.J., Tsou, S.K., McKeel, D.W., Morris, J.C., 2001. Neuron number in the entorhinal cortex and CA1 in preclinical Alzheimer disease. *Arch. Neurol.* 58, 1395–1402.
- Purger, D., McNutt, T., Achanta, P., Quiones-Hinojosa, A., Wong, J., Ford, E., 2009. A histology-based atlas of the C57BL/6J mouse brain deformably registered to in vivo MRI for localized radiation and surgical targeting. *Phys. Med. Biol.* 54 (24), 7315.

- Rangarajan, A., Chui, H., Mjolsness, E., Pappu, S., Davachi, L., Goldman-Rakic, P., Duncan, J., 1997. A robust point-matching algorithm for autoradiograph alignment. *Med. Image Anal.* 1 (4), 379–398.
- Rosazza, C., Minati, L., Ghilmetti, F., Maccagnano, E., Erbetta, A., Villani, F., Epifani, F., Spreafico, R., Bruzzone, M., 2009. Engagement of the medial temporal lobe in verbal and nonverbal memory: assessment with functional MR imaging in healthy subjects. *Am. J. Neuroradiol.* 30 (6), 1134–1141.
- Saleem, K., Logothetis, N., 2012. A Combined MRI and Histology Atlas of the Rhesus Monkey Brain in Stereotaxic Coordinates. Academic Press.
- Schormann, T., Dabringhaus, A., Zilles, K., 1995. Statistics of deformations in histology and application to improved alignment with MRI. *IEEE Trans. Med. Imaging* 14 (1), 25–35.
- Shepherd, T.M., Zarslan, E., Yachnis, A.T., King, M.A., Blackband, S.J., 2007. Diffusion tensor microscopy indicates the cytoarchitectural basis for diffusion anisotropy in the human hippocampus. *Am. J. Neuroradiol.* 28 (5), 958–964.
- Shing, Y.L., Rodrigue, K.M., Kennedy, K.M., Fandakova, Y., Bodammer, N., Werkle-Bergner, M., Lindenberger, U., Raz, N., 2011. Hippocampal subfield volumes: age, vascular risk, and correlation with associative memory. *Front. Aging Neurosci.* 3.
- Simic, G., Kostovic, I., Winblad, B., Bogdanovic, N., 1997. Volume and number of neurons of the human hippocampal formation in normal aging and Alzheimer's disease. *J. Comp. Neurol.* 379 (4), 482–494.
- Simmons, D.M., Swanson, L.W., 2009. Comparing histological data from different brains: sources of error and strategies for minimizing them. *Brain Res. Rev.* 60 (2), 349.
- Small, S.A., Nava, A.S., Perera, G.M., DeLaPaz, R., Mayeux, R., Stern, Y., 2001. Circuit mechanisms underlying memory encoding and retrieval in the long axis of the hippocampal formation. *Nat. Neurosci.* 4 (4), 442.
- Small, S.A., Schobel, S.A., Buxton, R.B., Witter, M.P., Barnes, C.A., 2011. A pathophysiological framework of hippocampal dysfunction in ageing and disease. *Nat. Rev. Neurosci.* 12 (10), 585–601.
- Squire, L.R., Stark, C.E., Clark, R.E., 2004. The medial temporal lobe. *Annu. Rev. Neurosci.* 27 (1), 279–306.
- Strange, B.A., Fletcher, P.C., Henson, R.N.A., Friston, K.J., Dolan, R.J., 1999. Segregating the functions of human hippocampus. *Proc. Natl. Acad. Sci.* 96 (7), 4034–4039.
- Suthana, N.A., Ekstrom, A.D., Moshirvaziri, S., Knowlton, B., Bookheimer, S.Y., 2009. Human hippocampal CA1 involvement during allocentric encoding of spatial information. *J. Neurosci.* 29 (34), 10512–10519.
- Thomas, B.P., Welch, E.B., Niederhauser, B.D., Whetsell, W.O., Anderson, A.W., Gore, J.C., Avison, M.J., Creasy, J.L., 2008. High-resolution 7 T MRI of the human hippocampus *in vivo*. *J. Magn. Reson. Imaging* 28 (5), 1266–1272.
- Toga, A.W., Goldkorn, A., Ambach, K., Chao, K., Quinn, B.C., Yao, P., 1997. Postmortem cryosectioning as an anatomic reference for human brain mapping. *Comput. Med. Imaging Graph.* 21 (2), 131–141.
- Van Leemput, K., Bakkour, A., Benner, T., Wiggins, G., Wald, L.L., Augustinack, J., Dickerson, B.C., Golland, P., Fischl, B., 2009. Automated segmentation of hippocampal subfields from ultra-high resolution *in vivo* MRI. *Hippocampus* 19 (6), 549–557.
- van Strien, N.M., Widere, M., van de Berg, W.D.J., Uylings, H.B.M., 2011. Imaging hippocampal subregions with *in vivo* MRI: advances and limitations. *Nat. Rev. Neurosci.* 13 (1), 70–70.
- Wang, L., Swank, J.S., Glick, I.E., Gado, M.H., Miller, M.I., Morris, J.C., Csernansky, J.G., 2003. Changes in hippocampal volume and shape across time distinguish dementia of the Alzheimer type from healthy aging. *Neuroimage* 200 (2), 667–682.
- West, M.J., Gundersen, H.J.G., 1990. Unbiased stereological estimation of the number of neurons in the human hippocampus. *J. Comp. Neurol.* 296 (1), 1–22.
- West, M.J., Coleman, P.D., Flood, D.G., Troncoso, J.C., 1994. Differences in the pattern of hippocampal neuronal loss in normal ageing and Alzheimer's disease. *Lancet* 344 (8925), 769–772.
- Wiesehmann, U.C., Symms, M.R., Mottershead, J.P., MacManus, D.G., Barker, G.J., Tofts, P.S., Revesz, T., Stevens, J.M., Shorvon, S.D., 1999. Hippocampal layers on high resolution magnetic resonance images: real or imaginary? *J. Anat.* 195 (1), 131–135.
- Winterburn, J.L., Pruessner, J.C., Chavez, S., Schira, M., Lobaugh, N.J., Voineskos, A.N., Chakravarty, M.M., 2013. A novel *in vivo* atlas of human hippocampal subfields using high-resolution 3 T magnetic resonance imaging. *Neuroimage* 254–265.
- Wisse, L., Gerritsen, L., Zwanenburg, J., Kuijf, H., Luijten, P., Biessels, G., Geerlings, M., 2012. Subfields of the hippocampal formation at 7 T MRI: *in vivo* volumetric assessment. *Neuroimage* 61 (4), 1043–1049.
- Xiao, G., Bloch, B.N., Chappelow, J., Genega, E.M., Rofsky, N.M., Lenkinski, R.E., Tomaszewski, J., Feldman, M.D., Rosen, M., Madabhushi, A., 2011. Determining histology-MRI slice correspondences for defining MRI-based disease signatures of prostate cancer. *Comput. Med. Imaging Graph.* 35 (7), 568–578.
- Yassa, M.A., Stark, S.M., Bakker, A., Albert, M.S., Gallagher, M., Stark, C.E., 2010. High-resolution structural and functional MRI of hippocampal CA3 and dentate gyrus in patients with amnestic mild cognitive impairment. *Neuroimage* 51 (3), 1242–1252.
- Yelnik, J., Bardinet, E., Dormont, D., Malandain, G., Ourselin, S., Tandé, D., Karachi, C., Ayache, N., Cornu, P., Agid, Y., 2007. A three-dimensional, histological and deformable atlas of the human basal ganglia. I. Atlas construction based on immunohistochemical and MRI data. *Neuroimage* 34 (2), 618–638.
- Yong-Hing, C.J., Obenaus, A., Stryker, R., Tong, K., Sarty, G.E., 2005. Magnetic resonance imaging and mathematical modeling of progressive formalin fixation of the human brain. *Magn. Reson. Med.* 54 (2), 324–332.
- Yushkevich, P., Avants, B., Ng, L., Hawrylycz, M., Burstein, P., Zhang, H., Gee, J., 2006a. 3D mouse brain reconstruction from histology using a coarse-to-fine approach. *Lect. Notes Comput. Sci.* 4057, 230–237.
- Yushkevich, P.A., Piven, J., Cody Hazlett, H., Gimpel Smith, R., Ho, S., Gee, J.C., Gerig, G., 2006b. User-guided 3D active contour segmentation of anatomical structures: significantly improved efficiency and reliability. *Neuroimage* 31 (3), 1116–1128.
- Yushkevich, P., Avants, B., Pluta, J., Das, S., Minkoff, D., Mechanichamilton, D., Glynn, S., Pickup, S., Liu, W., Gee, J., 2009. A high-resolution computational atlas of the human hippocampus from postmortem magnetic resonance imaging at 9.4 T. *Neuroimage* 44 (2), 385–398.
- Yushkevich, P.A., Wang, H., Pluta, J., Das, S.R., Craige, C., Avants, B.B., Weiner, M.W., Mueller, S., 2010. Nearly automatic segmentation of hippocampal subfields in *in vivo* focal T2-weighted MRI. *Neuroimage* 53 (4), 1208–1224.
- Zeineh, M.M., Engel, S.A., Bookheimer, S.Y., 2000. Application of cortical unfolding techniques to functional MRI of the human hippocampal region. *Neuroimage* 11 (6), 668–683.
- Zeineh, M.M., Holdsworth, S., Skare, S., Atlas, S.W., Bammer, R., 2012. Ultra-high resolution diffusion tensor imaging of the microscopic pathways of the medial temporal lobe. *Neuroimage* 62 (3), 2065–2082.
- Zola-Morgan, S., Squire, L.R., 1993. Neuroanatomy of memory. *Annu. Rev. Neurosci.* 16, 547–563.